

## REVIEW

[View Article Online](#)  
[View Journal](#) | [View Issue](#)

Cite this: *Mater. Adv.*, 2021,  
2, 7502

## Recent advances in ultra-low temperature (sub-zero to 100 °C) synthesis, mechanism and applications of titania (TiO<sub>2</sub>) nanoparticles

Kiran P. Shejale,<sup>ab</sup> R. Krishnapriya,<sup>bc</sup> Harshala Patil,<sup>d</sup> Devika Laishram,<sup>be</sup> Pratyush Rawal<sup>f</sup> and Rakesh K. Sharma<sup>id</sup>\*<sup>b</sup>

The development of titania (TiO<sub>2</sub>) nanomaterials for next-generation photonic, optoelectronic, and catalytic applications necessitates a facile and cost-effective synthetic methodology for precisely tuning the composition, phase, and morphology at nanometer scales. In this review, an attempt has been made to comprehend the progress of the emerging and rapidly developing synthesis methods evolved for the low-temperature synthesis of titania with a particular emphasis on sub-zero temperature. Insights and understandings of how the temperature affects the characteristic surface properties and morphology of titania, along with a detailed discussion on the material characteristics for various technological device applications are dealt with various methods of analysis. Furthermore, the temperature-dependent morphological (0D–3D) and structural changes and their impact on different energy-harvesting and storage and water remediation applications are elucidated. Thus, this review specifically opens the understanding of different TiO<sub>2</sub> polymorph syntheses and their physiochemical comprehension for advanced technological device performance enhancement.

Received 11th October 2021,  
Accepted 16th October 2021

DOI: 10.1039/d1ma00942g

[rsc.li/materials-advances](https://rsc.li/materials-advances)

<sup>a</sup> *Mechanics and Electrochemistry of Functional Materials (MEFM) Laboratory, School of Mechanical Engineering, Kyungpook National University, Daegu, 41566, South Korea*

<sup>b</sup> *Sustainable Materials and Catalysis Research Laboratory (SMCRL), Department of Chemistry, Indian Institute of Technology Jodhpur, Jodhpur, 342037, India. E-mail: rks@iitj.ac.in*

<sup>c</sup> *Mechanical Engineering Department, College of Engineering, United Arab Emirate University, Al Ain 15551, United Arab Emirates*

<sup>d</sup> *Centre for Technology Alternatives for Rural Areas, Indian Institute of Technology Bombay, Powai, Mumbai, 400076, India*

<sup>e</sup> *University College Dublin, School of Chemical and Bioprocess Engineering, Engineering Building, Belfield, Dublin 4, Ireland*

<sup>f</sup> *Department of Electrical, Computer and Energy Engineering, University of Colorado Boulder, 425 UCB Boulder, CO 80309, USA*



**Kiran P. Shejale**

*energy harvesting, storage, electrochemical devices, biosensors, catalysis and water, and air remediation.*

*Dr Shejale is a Postdoctoral Fellow at KNU, South Korea. He completed his PhD from IIT Jodhpur, MTech from IIT Roorkee, India, and PDF from IIT Bombay. He received a gold medal for the best paper at the Optics'14 international conference. He has authored more than 21 international research articles and 5 patents. His interdisciplinary research area includes material chemistry, carbon materials, advanced nanomaterials for*



**R. Krishnapriya**

*and the application of transition metal-based catalytic systems for the biomass up-gradation and related value-added products conversion.*

*Dr Krishnapriya is currently a Postdoctoral Fellow at Mechanical Engineering Department, United Arab Emirate University, Al Ain 15551, UAE. She also worked as a Postdoctoral Fellow at the Department of Chemistry at the Indian Institute of Technology, Jodhpur, India. She obtained a PhD degree in Chemistry from Pondicherry University in 2017. Her research interests include the development of nanostructured materials for solar photovoltaics,*



# 1. Introduction

Nano-structured materials have garnered much scientific attention these days throughout the world, owing to their distinctive properties. Among the various nanostructured functional materials of all transition metal oxides,  $\text{TiO}_2$  found an advantageous position. Titanium dioxide is also known as titanium(IV) dioxide, titania or  $\text{TiO}_2$ , E171 food colour or pigment white 6.<sup>1–4</sup> The application potential of this material was first widely identified after Fujishima and Honda discovered the photolysis of water

using  $\text{TiO}_2$  as a photocatalyst.<sup>5</sup> The photo killing of few notorious bacteria such as *E. coli*, *L. acidophilus*, and *S. cerevisiae* by the photocatalytic property, further inhabiting the malignant (HeLa), biocompatibility, environmental friendliness, and huge potential for the emerging fields (such as solar cells, water–air remediation, and others) have made this material ( $\text{TiO}_2$ ) the most investigated semiconductor to solve many significant challenging themes of mankind that are requisite to be addressed in this century.<sup>6,7</sup>

Several exceptional characteristics have been demonstrated by  $\text{TiO}_2$ , such as a wide bandgap, physiochemical



**Harshala Patil**

*Dr Patil is working at the Water Innovation Center: Technology & Education as a Senior Project Officer. She obtained her M. Tech from IIT Kharagpur, India, and subsequently worked with G. G. Dandekar Pvt., Ltd as an Assistant Manager in the R&D Department. She completed her PhD from IIT Bombay, India. Her research interests include the quality of food and water, food and water testing, an antibiotic study in water, policy-making and recommendations for pollutants in water and losses during the supply chain of food.*



**Devika Laishram**

*Dr Laishram received her PhD from the Indian Institute of Technology Jodhpur, where she worked with Dr Rakesh K. Sharma. She has a Master's degree from Pondicherry University in Nanoscience and Nanotechnology. She was awarded the Science and Engineering Research Board (SERB) – Overseas Visiting Doctoral Fellowship (OVDF) 2018–19 to carry out 6 months of research at the University of Alberta, Canada by SERB, Department of Science and Technology (DST), India. Her research work is mainly focused on devising new materials for energy and environmental applications, such as solar energy harvesting and storage, catalytic oxidation of soot, treatment of industrial dyes, water splitting and  $\text{CO}_2$  capture. Currently, she is working as a Research Associate with Prof. Rakesh K. Sharma at IIT Jodhpur.*



**Pratyush Rawal**

*Mr Rawal is an Electrical Engineer currently working at Motiv Power Systems in California, USA. He received his Master of Science degree in Electrical Engineering from the University of Colorado Boulder, USA. He worked as an intern at the Indian Institute of Technology Jodhpur, working on Perovskite Solar Cells with Dr Rakesh Kumar Sharma and Dr Kiran P. Shejale. His research interests include electric vehicles, renewable energy sources, and the future power grid using solar and wind energy.*



**Rakesh K. Sharma**

*Dr Sharma is an Associate Professor at the Department of Chemistry at IIT Jodhpur, India. He received his BSc and MSc from the University of Rajasthan Jaipur, and PhD from the Indian Institute of Science Bangalore in 2008. He worked as a post-doctoral researcher from 2008 to 2010 at the Ohio State University. He has published 3 awarded Indian patents and 5 filed patents. He has published more than 100 journal articles in peer-reviewed journals, including Journal of American Chemical Society, Chemical Science, ACS Sustainable Eng. and Chemistry, to name a few. He has also published 9 books/book chapters. His research interests include catalysis for biofuels and fine chemicals, Rajasthan clay catalyst, plasma catalysis for environmental remediation, and advanced materials for energy generation and storage.*



characteristics (e.g., high thermal and chemical stability), excellent environmentally friendly nature and earth-abundance, among others. Such factors marked this material as one of the versatile components in several diversified fields, such as cosmetics, UV sunscreens, pigments, metallurgy, solar energy harvesting, hydrogen generation, catalysis, sensors, biomedical implants, and others.<sup>8–11</sup> Many unprecedented properties of TiO<sub>2</sub>, such as the morphology, phase composition, size and surface area, have a major effect on various physicochemical properties of the material, viz., particle size, hollow structures, 0D–3D, hierarchical, and micro-sized spheres. This further drove more attention for rigorous structural optimization efforts to achieve better applications.<sup>2,12–14</sup>

Commercially, TiO<sub>2</sub> is applied in a widespread manner in different fields as a prevalent nanomaterial.<sup>3</sup> Importantly, external factors of the environment during the process (pressure and temperature) determine the structure of TiO<sub>2</sub> NPs, which ultimately decides its functional characteristics and usage. Moreover, TiO<sub>2</sub> phase stability is a significant factor for its potential applications. Essential properties of TiO<sub>2</sub> NPs for different applied fields are varied as per the mode of usage; for example, in biomedical TiO<sub>2</sub> NPs, the mechanical properties (elasticity, mechanical compatibility, and deformation behaviour) play a very crucial role.<sup>3,4</sup>

Various synthetic strategies have been explored to reinforce TiO<sub>2</sub>, such as sol–gel, hydrothermal, RF sputtering, laser ablation, mechano-chemical and many more. Specifically, these approaches are based on certain design principles, such as certain phase-orientations, morphology, band structure and increasing the active sites.<sup>15,16</sup> In the beginning, much of the focus has been given to 1D nano TiO<sub>2</sub>. A higher surface area and better quantum size were reported, along with easy and trouble-free preparation steps. Subsequently, 2D nano TiO<sub>2</sub> has emerged as being comparatively difficult in terms of the preparation process. Different synthetic and improved paths were applied to defeat these two obstacles and advance the performance of nano TiO<sub>2</sub>. It included improvement in the surface properties, introduction of novel materials for making a hierarchical structure, and a change in the internal crystal structure.<sup>4</sup> Furthermore, the above methods for TiO<sub>2</sub> nanoparticles have possessed high energy consumption, complexity, environmental impact, and robust steps like high pressure–temperature, prolonged production time and low production disadvantages.<sup>17</sup> Therefore, it was a primary interest to have a simple process with large scale potential for the low production cost. Among all, the thermal aspect of the synthetic process becomes significantly important, especially for biotechnological applications. This is due to the thermal degradation tendency in that functional nanomaterials cannot be processed at elevated temperature.<sup>18</sup> Moreover, constructing functional nano TiO<sub>2</sub>, considering the thermal aspect (especially at low temperature), can compensate the drawbacks of the other preparation methods by a certain extent. This will benefit the synergistic outcome between the physiochemical properties and utilizing it for several applications. Thermal variation has become one of the crucial parameter for TiO<sub>2</sub> synthesis in a controlled manner for diverse morphology, phase and property.<sup>19</sup>

Of late, there are many review articles on the synthesis of titania.<sup>20–25</sup> Most of them discuss either the synthesis process, morphological tuning, or the application possibilities in detail. However, an inclusive review on the low-temperature synthesis of titania detailing its specific importance, understanding the fabrication of different TiO<sub>2</sub> polymorphs, and comprehending its physiochemical properties have not yet been explored. In this context, this review focuses on filling this gap and tries to bridge a strong connection between the novel low-temperature synthesis techniques to fabricate titania, and its significance in scale-up for advanced technological device applications.

## 1.1 Titania

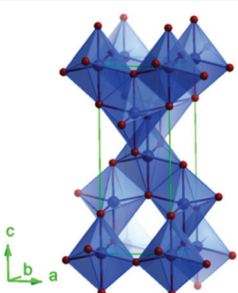
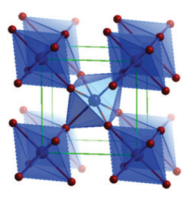
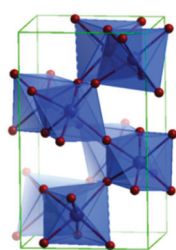
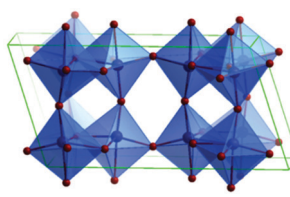
Predominantly, four crystalline structures of titania nanoparticles are found in nature (space groups in parentheses), viz., anatase (tetragonal, (*I41/amd*)), rutile (tetragonal, (*P4/mnm*)), brookite (orthorhombic, (*Pbca*)) and TiO<sub>2</sub>(B) (monoclinic, (*C2/m*)).<sup>26–28</sup> Additionally, there are other crystalline forms of titania (synthetic polymorphs): tetragonal TiO<sub>2</sub>(H) orthorhombic TiO<sub>2</sub>(R) and high-pressure forms, such as orthorhombic TiO<sub>2</sub>(II) (*Pbcn*), monoclinic, orthorhombic TiO<sub>2</sub>–OI (*Pbca*), baddeleyite (*P21/c*), cubic and orthorhombic TiO<sub>2</sub>–OII phases.<sup>29–32</sup> Moreover, ramsdellite (*Pbnm*) and hollandite (*I4/m*) are observed under high pressure as the nanoporous phases.<sup>33,34</sup> These phases are different based on the connectivity of the polyhedra, coordination of O, distortion of octahedra, and order of arrays of TiO<sub>6</sub>. Furthermore, relevant structural data of the synthetic polymorphs can be seen at publicly available databases.<sup>34</sup> Among these, the anatase and rutile phases exhibit very similar physical properties like a wide band-gap of 3.0–3.2 eV, which is capable of reflecting visible light. Table 1 summarizes the various properties of the titania nanoparticles in different crystalline structures.

Fundamental building blocks are used to demonstrate the different TiO<sub>2</sub> phases using Ti–O octahedrons by crystal diagram (Table 1). Different symmetries are shown by all of these TiO<sub>2</sub> phases. The lowest energy is carried by tetragonal rutile (*a* = 0.459 nm, *c* = 0.296 nm corresponding to the (011) and (100) planes). Anatase has a tetragonal structure with slightly different dimensions (*a* = 0.379 nm, *c* = 0.951 nm).<sup>35</sup> The orthorhombic structure of brookite has eight groups of TiO<sub>2</sub>. TiO<sub>2</sub>(B) has the largest monoclinic cell (*a* = 1.216 nm) and has a more open crystal structure compared to other structures.<sup>36</sup> However, brookite and TiO<sub>2</sub>(B) phases are seldom witnessed during nano TiO<sub>2</sub> synthesis. Perovskite, TiO<sub>2</sub>(H) and TiO<sub>2</sub> II are metastable polymorphs and strained structures. Various phases have different characteristics. Desired morphologies are attained by maintaining specific conditions during synthesis. Titanium ions are six-fold coordinated to oxygen anions in a single structural unit, which establish the TiO<sub>6</sub> octahedral structure.<sup>37</sup> The octahedral arrangement is formed due to the crystallographic structure of the material. TiO<sub>2</sub>(B), anatase, and brookite are metastable, while rutile is the most stable structure due to its quadratic space group. Metastable materials are converted into rutile during heating. Nonetheless, these three metastable materials obtain the most stable state on the nanoscale, owing to the small surface energy. It is an open crystalline structure as





**Table 1** Various characteristic properties of anatase, rutile, brookite and TiO<sub>2</sub> (B)<sup>1,9,10</sup> (reproduced with permission.<sup>8</sup> Copyright 2014, American Chemical Society)

Properties	Anatase	Rutile	Brookite	TiO <sub>2</sub> (B)
Schematic unit cell				
Crystal structure	Tetragonal	Tetragonal	Orthorhombic	Monoclinic
Space group, unit cell parameters (nm)	<i>I41/amd</i> , $a = b = 0.379$ & $c = 0.951$	<i>P42/mnm</i> , $a = b = 0.459$ & $c = 0.296$	<i>Pbca</i> , $a = 0.918$ , $b = 0.545$ & $c = 0.515$	<i>C2/m</i> , $a = 1.216$ , $b = 0.374$ & $c = 0.651$ , $\beta = 107.3^\circ$
Ti–O bond length (Å)	1.937(4) 1.965(2)	1.949 (4) 1.980 (2)	1.87–2.04	2.20–2.25
Polyhedra per unit cell	4	2	8	8
Polyhedra per unit cell volume (1 Å <sup>3</sup> )	0.02936	0.03203	0.03108	0.02815
Density (g cm <sup>−3</sup> )	4.248	3.895	4.123	3.734
O–Ti–O bond angle	77.7° 92.6°	81.2° 90.0°	77.0°–105°	110.2–168.2°
Band gap (eV)	3.4	3	1.9	—
Dielectric constant	31	114	14–110	—
Refractive index	2.55	2.75	2.583–2.70	—
Mohr's hardness	5.5	6.5 to 7	5.5–6.0	—

an intermediate product of roasting titanite to anatase. Major photocatalytic and photovoltaic devices consist of anatase and rutile with band gaps of 3.2 and 3.0 eV, respectively.<sup>4</sup>

Li *et al.* carried out a comprehensive study of the process of phase transformation of anatase to rutile.<sup>38</sup> TiO<sub>2</sub> anatase particles agglomerate from interfaces during phase transformation, which lead to bulk phase transformation and growth of particle sizes. This transformation depends on many factors, such as defect sites and particle size of the initial anatase. The phase transformation is brookite, followed by anatase, followed by rutile transition.<sup>39</sup> During the brookite-to-anatase transition, a quasi-H<sub>2</sub>Ti<sub>3</sub>O<sub>7</sub> structure is observed by UV Raman spectroscopy. The TiO<sub>2</sub>(B)-to-rutile transition undergoes a phase transformation by getting anatase as a middle phase.<sup>8</sup>

In the band structure of TiO<sub>2</sub>, O 2p orbitals contribute to the filled valence band (VB), while Ti 3d, 4s, 4p orbitals contribute to the unoccupied conduction band (CB). Ti 3d orbitals dominate the lower position of CB.<sup>40,41</sup> Optimization of the optical and electronic structures of TiO<sub>2</sub> is a crucial point to reduce the higher recombination rate compared to separation rate. Changes in the band structure and increase in e<sup>−</sup> life can both be achieved by doping other elements as the photoinduced carriers. Cation doping in place of Ti increases the impurity, and the intermediate energy level could act as an e<sup>−</sup> donor or acceptor, which permits TiO<sub>2</sub> to absorb visible light.<sup>8</sup> Fig. 1a reveals the energy band gap ( $E_g$ ) positions and values of various TiO<sub>2</sub> polymorphs determined from plane-wave DFT, which are in accordance with the experimental findings. These values are associated with the redox potentials of H<sub>2</sub>O with reference to the standard hydrogen electrode potential  $E(\text{H}^+/\text{H}_2) = 4.44$  V

and H<sub>2</sub>O splitting free energy (1.23 eV) relative to a vacuum at room temperature. Fig. 1a demonstrates the variation in the bandgap, ionization potential and electron affinity for the TiO<sub>2</sub> eight polymorphs. The baddeleyite phase reveals that the exceptionally high valence band position (4.77 eV, low ionization potential) and lower electron affinity (2.57 eV, work function) differs from other polymorphs with Ti coordination (seven as opposed to six), and mix with two- and four-coordinated O (TiO<sub>2</sub>-B also shares same).<sup>42</sup> As shown in the electronic density of states in Fig. 1b, the valence bond of TiO<sub>2</sub> is predominately derived from the overlapping O 2p-like states. The Madelung potential (VM) and Mott and Littleton approaches have been explored to analyze the dynamic polarization of the crystal from all polymorphs, and the hole on an oxygen site formation was simulated as an ionization process.

Enhancement of the photocatalytic activity and physico-chemical properties can be carried out by the crystal facet engineering of TiO<sub>2</sub>. The dominant facets for rutile are 110, 100, and 101. Meanwhile, 101 and 001 are the dominant facets for anatase. Of these, 110 possesses the lowest energy because it has been studied comprehensively.<sup>43</sup> For anatase TiO<sub>2</sub>, scientists have demonstrated that the 001 facet possesses a large number of under-bonded Ti atoms and large Ti–O–Ti bond angles.<sup>8</sup>

In particular, the anatase phases of titania can reflect a wider electro-magnetic spectrum covering the long-wave ultraviolet (UVA) light besides visible light. On the other hand, rutile TiO<sub>2</sub> nanoparticles can absorb violet visible light. Thus, these two forms find potential applications in the area of photocatalysis, owing to its unique photo-induced charge transfer mechanisms.<sup>44</sup>





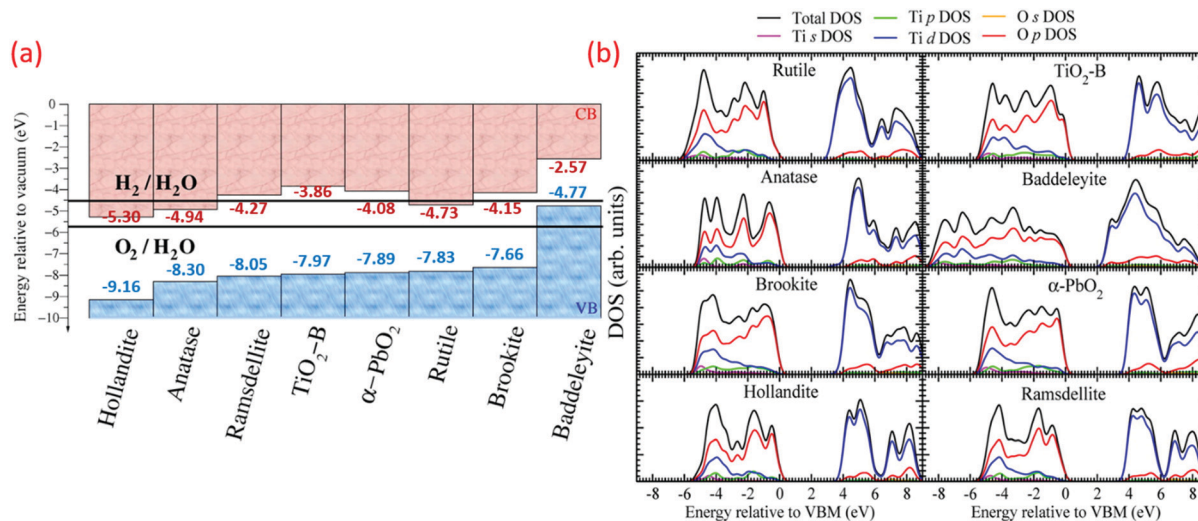


**Fig. 1** (a) Valence band (VB) and conduction band (CB) positions ( $\text{H}_2$  and  $\text{O}_2$  redox potentials mentioned for comparison), and (b) electronic density of states (DOS) and partial DOS derived from s, p, and d orbital contributions of various  $\text{TiO}_2$  polymorphs (reproduced with permission.<sup>42</sup> Copyright 2015, American Chemical Society).

Recently, the nanostructured  $\text{TiO}_2$  has attracted more consideration owing to its high surface-volume ratio, which induces much more photo-induced reactions that enhance the light absorption. Furthermore, its high surface photoinduced carrier generations result in improving the photo-reduction rate.<sup>45,46</sup> Thus, nanostructured titania can significantly improve the surface photoactivity. The high surface-volume ratio of the nanostructured titania proved to enhance the  $\text{OH}^-$  and  $\text{H}_2\text{O}$  surface absorption, thus increasing the photocatalytic reaction rate.<sup>47</sup>

## 1.2 Low temperature (room temperature) as a key

Recent nano-technological advancement enabled researchers to produce different nanomaterials and nanoparticles, which have applications in cosmetics, textiles, construction and building products, electronics, energy, paints, healthcare, water purification and remediation, inks, optics, paper, and others.<sup>35,44,48</sup>

There are many strategies to synthesize nanoparticles and submicron size materials, such as microwave-based techniques, sol-gel processing, laser ablation, mechanical and mechanochemical processing, chemical precipitation, chemical vapour deposition, flame-assisted synthesis, rapid expansion of supercritical liquid solution, and others.<sup>1,3,39,49</sup> Many disadvantages have been reported for these methods, such as their environmentally-unfriendly nature, complex methodology, high process time, high energy consumption, and small scale production (0.1 to 1 kg per day), leading to very high costs.<sup>29,50,51</sup> The development of sustainable processes that could produce large scale nanomaterials at low cost with simple operations, better quality/properties, and lower temperature is a need of the hour.<sup>11</sup>

Different production methods, such as laser, aerosol, inert gas, hydrothermal, and sol-gel, have been reported by researchers for the fabrication of titania nanostructures in different morphologies and structures, such as tubes, crystals, wires and rods.<sup>11,36,52</sup> Below room temperature-controlled reactions of

highly reactive titanium precursors led to variable crystalline structures.<sup>19</sup> A few researchers found that controlled hydrolysis with surfactants acquires precise growth of nano  $\text{TiO}_2$ .<sup>2,13,14</sup> However, a few operations produce better performing nano  $\text{TiO}_2$  with distinct process parameters, such as high calcination temperature, high temperature, and ultra-high vacuum, which make these processes complicated.<sup>19</sup>

Nanostructures of  $\text{TiO}_2$  were fabricated by different synthetic strategies (physical mixing, annealing and doping) to achieve altered morphology and ultimately physical properties.<sup>1,53</sup> Previously, titania was prepared commercially at higher temperature or highly acidic/basic synthetic conditions. Such cumbersome operations led to observed adverse phase transformations restraining its applications.<sup>54,55</sup> At low temperature, insightful modification in the process temperature could produce the controlled growth of nano  $\text{TiO}_2$ .<sup>2</sup>

Simple, easy, ambient temperature-driven and additive-free synthesis protocols for the better quality of nano  $\text{TiO}_2$  are a persuasive priority. Temperature is one of the significant factors that determine the nanostructure and physiochemical properties of  $\text{TiO}_2$ . Various researchers reported the preparation of three different phase  $\text{TiO}_2$  nanomaterials, such as anatase, rutile and brookite, at lower temperature using sol-gel protocol.<sup>56–58</sup> Room temperature, *i.e.*, 25 °C, is commonly considered as a low temperature in most of the related findings.<sup>11,59</sup> A temperature of 4 °C is the lowest reported temperature for the preparation of  $\text{TiO}_2$  nanomaterials, while sub-zero temperature studies are scanty.<sup>19</sup> The morphology and intrinsic electronic structure depend on the phase and operating temperature during the preparation of  $\text{TiO}_2$ , which ultimately determines the physical and chemical properties of nano  $\text{TiO}_2$  (Fig. 1). Different applications utilized various nano  $\text{TiO}_2$  structures consisting of distinct morphologies 0D to 3D (nanotubes, nanorods, nanofibers, nanosheets, and interconnected architectures) and related unique properties. The maximum



particle amalgamation mainly caused by annealing. Therefore, for the preparation of smaller nanoparticles of  $\text{TiO}_2$ , low-temperature synthetic strategies have great importance.<sup>49,60</sup> Hence, it is crucial to control the synthesis temperature as it has a direct significant diverse effect on the physiochemical properties of  $\text{TiO}_2$ .

A brief history of the development of  $\text{TiO}_2$  materials with the timeline prepared at low temperature ( $-196$  to  $100\text{ }^\circ\text{C}$ ) toward the varied nanostructures is given in Fig. 2. Although developments in the low-temperature synthesis of nano  $\text{TiO}_2$  have been substantial for a few years, applications with satisfactory results have been lacking. There is a large temperature gap during synthesis ( $25$  to  $100\text{ }^\circ\text{C}$ ) and the literature is absent for the synthesis of nano  $\text{TiO}_2$  at real sub-zero or  $<100\text{ }^\circ\text{C}$  temperature. Various researchers have published reviews with regards to a multitude of materials including  $\text{TiO}_2$  through a widespread arena of fields.<sup>61,62</sup> Nevertheless, a comprehensive review of the design, fabrication, and clarification of a large variety of various morphologies, phase, and most importantly low temperature (sub-zero to  $-100\text{ }^\circ\text{C}$ ), along with their multipurpose uses is sparse. This is of utmost significance to researchers in transition metal oxides.<sup>9,37,63</sup> Additionally, the objective assessment of low temperature effects on the different size, shape and phase-based synthesis methods of nano  $\text{TiO}_2$ , synthesis procedures has not

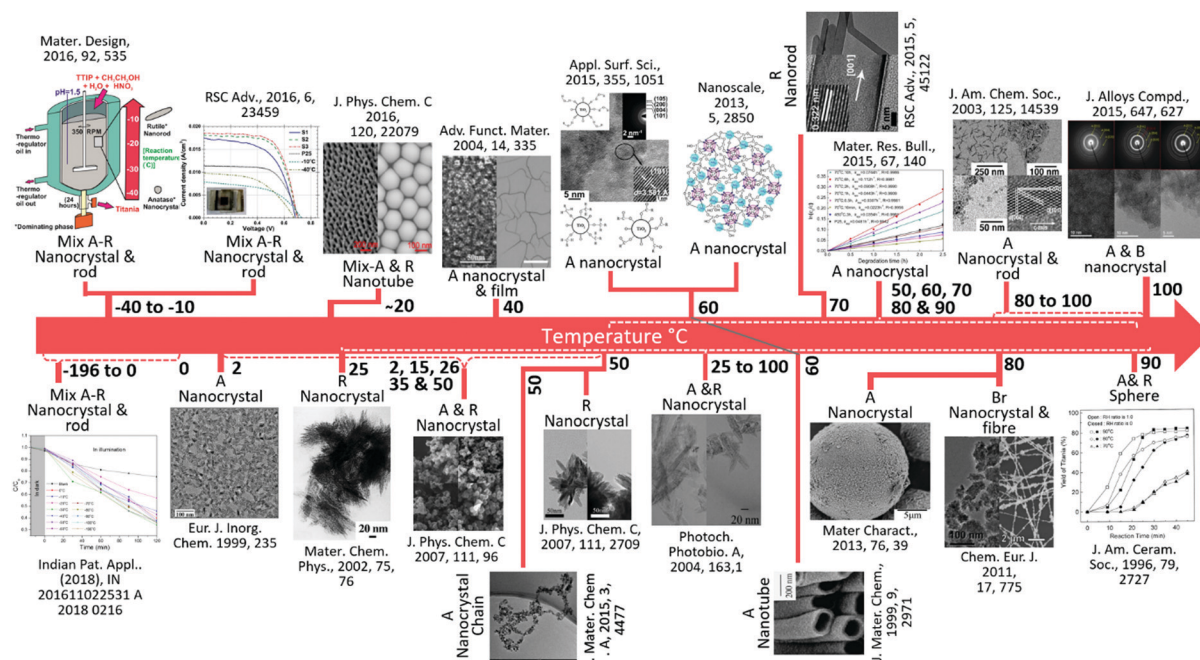


**Fig. 2** A brief summary of the key development of TiO<sub>2</sub> materials at low temperature (−196 to 100 °C). A, R, B and Br represent anatase, rutile, brookite and bronze, respectively. From left to right, (reproduced with permission.<sup>19</sup> Copyright 2016, Elsevier), (reproduced with permission.<sup>64</sup> Copyright 1999, John Wiley and Sons), (reproduced with permission.<sup>65</sup> Copyright 2016, American Chemical Society), (reproduced with permission.<sup>66</sup> Copyright 2002, Elsevier), (reproduced with permission.<sup>67</sup> Copyright 2004, John Wiley and Sons), (reproduced with permission.<sup>68</sup> Copyright 2007, American Chemical Society), (reproduced with permission.<sup>69</sup> Copyright 2015, Royal Society of Chemistry), (reproduced with permission.<sup>70</sup> Copyright 2007, American Chemical Society), (reproduced with permission.<sup>71</sup> Copyright 2013, Royal Society of Chemistry), (reproduced with permission.<sup>72</sup> Copyright 2004, Elsevier), (reproduced with permission.<sup>73</sup> Copyright 1999, Royal Society of Chemistry), (reproduced with permission.<sup>74</sup> Copyright 2015, Royal Society of Chemistry), (reproduced with permission.<sup>75</sup> Copyright 2016, Elsevier), (reproduced with permission.<sup>76</sup> Copyright 2013, Elsevier), (reproduced with permission.<sup>77</sup> Copyright 2003, American Chemical Society), (reproduced with permission.<sup>78</sup> Copyright 2011, John Wiley and Sons), (reproduced with permission.<sup>79</sup> Copyright 2015, Elsevier), (reproduced with permission.<sup>80</sup> Copyright 2005, John Wiley and Sons).

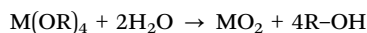
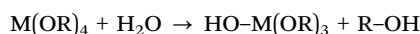
been reported adequately. Here, in this review paper, a detailed discussion regarding the preparations and fabrications of nano TiO<sub>2</sub> structures is presented, along with the synthesis conditions and regulatory accountability of morphologies. The physical, electronic, electrical, and optical properties of the TiO<sub>2</sub> nanostructure are also conferred. The latest research regarding the preparation and applications of nano TiO<sub>2</sub> is given along with future perspectives for boosting the physicochemical properties of TiO<sub>2</sub> at low temperature, and their potential for various applications are summarized.

## 2. Synthetic Strategies for TiO<sub>2</sub> nanostructures at low temperature

TiO<sub>2</sub> synthesis methods include physical (sol-gel, micelle, vapor deposition), chemical (sonochemical), electrical (electrodeposition), and thermal (hydrothermal, solvothermal, microwave).<sup>15,59,81,82</sup> The process parameters of synthesis, such as additives, temperature, ageing, acidity, and solvent, determine the size, phase and structure of the TiO<sub>2</sub> nanomaterials.<sup>49</sup> The large-scale synthesis of TiO<sub>2</sub> under high acidic/basic conditions and high temperatures is usually accompanied by undesirable phase transformations that confine the wide applicability of this material. Thus, various attempts were adopted to synthesize functional TiO<sub>2</sub> nanoparticles *via* the modest, but perspicacious change in reaction temperature that could lead to the thermodynamically controlled growth of the crystals.<sup>83–85</sup>

### 2.1 Sol-gel

Generally, the sol-gel method is used to produce solids from minute molecules in a process that involves hydrolysis, and is followed by polycondensation reaction of the precursors to form a colloid that is commonly named as 'sol'. Typical precursors used for the synthesis are metal alkoxides and metal chlorides. Subsequently, various metal oxides can be successfully obtained by this method, as shown in Fig. 3a. A generalized reaction for the sol-gel process is shown below.



where M can be Ti, Si or any other semiconductor, and OR is the alkoxide group. Alkoxide or RO<sup>−</sup> groups are good nucleophiles and thus strong bases. When mixed in water, they readily donate an electron and displace hydrogen from water to form HO-M(OR)<sub>3</sub>, which is the result of partial hydrolysis. This intermediate compound can combine with M(OR)<sub>4</sub> and form (OR)<sub>3</sub>-M-O-M-(OR)<sub>3</sub>. Thus, polymerization takes place which if completed, can convert liquid sol into a solid gel.<sup>86,87</sup> The wide applicability of this synthesis technique is due to its simplicity and quickness with water being the only byproduct.<sup>13,14</sup> An acid catalyzed sol-gel method is reported specifically for the nanostructured titania synthesis during which titanium alkoxide undergoes direct hydrolysis in the presence of an acetic acid catalyst at low temperature in the range of 25 to 80 °C.<sup>86,88</sup> The

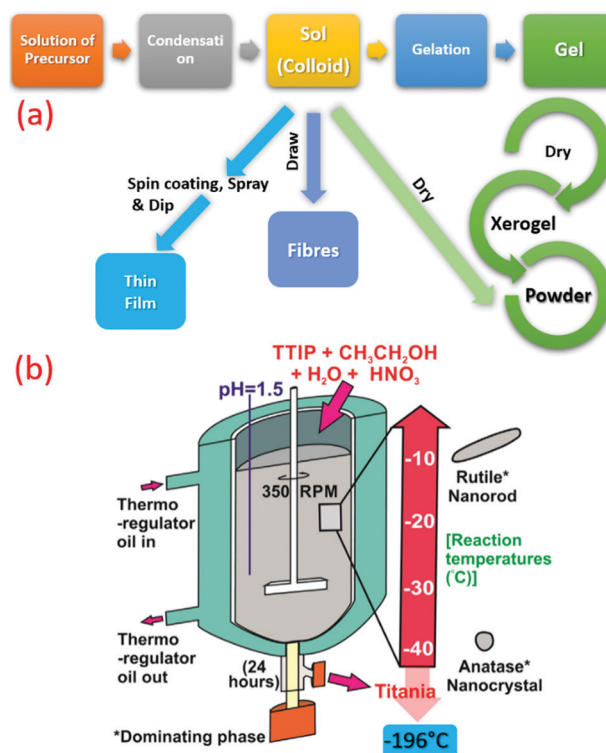


Fig. 3 (a) Summarized flow chart of TiO<sub>2</sub> synthesis by sol-gel technique at low temperature. (b) Schematic illustration of TiO<sub>2</sub> synthesis at sub-zero temperature (−196 to −10 °C) (reproduced with permission.<sup>19</sup> Copyright 2016, Elsevier).

reaction method developed was quite fast (under 3 h) and produced a large amount of hydroxylated titanium. The white polymer mass of hydroxylated titanium under constant stirring provides a colloidal white precipitate joined by van der Waals force of attraction. These colloidal nanoparticles at high nucleation rate produce amorphous titanium.

Another interesting study involved the synthesis of TiO<sub>2</sub> at room temperature using titanium *n*-butoxide and hydrochloric acid to produce the higher rutile phase.<sup>85</sup> By changing the temperature and acidity of the reaction, the shape of particles formed during the reaction can be varied. Wang *et al.* found that the direct hydrolysis of TiCl<sub>4</sub> with ethanol solution in water can yield rutile nanorods at a low temperature of 50 °C.<sup>70</sup> A slow hydrolysis method was also used by Cui *et al.* using TTIP and glacial acetic acid at a further low temperature of 50 °C.<sup>69</sup> The study revealed that the presence of a large amount of carboxylic acid promotes the polycondensation reaction. The nanocrystals of mesoporous anatase TiO<sub>2</sub> were also produced through heat treatment using water as a solvent in which the amorphous TiO<sub>2</sub> was obtained using tetra-butyl titanate as the precursor. The amorphous to crystalline phase change was achieved at temperatures above 50 °C. Huang *et al.* tried ultrasound irradiation to synthesize TiO<sub>2</sub> nanoparticles using a short crystalline time.<sup>89</sup>

Microwave-assisted sol-gel process produced very stable and monodisperse nano TiO<sub>2</sub> at 80 °C by using nitric acid and TTIP. The effect of different process parameters, *viz.*, time, catalyst concentration, temperature, was studied.<sup>90</sup> High temperatures





(40–100 °C) produced mesoporous rutile nano TiO<sub>2</sub> after 24 h using Ti(SO<sub>4</sub>)<sub>2</sub> and sulphuric acid TiO<sub>2</sub>-based sol.<sup>91</sup> Acid-catalyzed sol-gel method was used for producing TiO<sub>2</sub> *via* TEOS and MTES at 25 °C.<sup>92</sup> In another case, thin films of TiO<sub>2</sub> nanorods, nanowires, and nanoflowers were formed on metallic Ti substrates in aqueous hydrogen peroxide solution (80 °C, 72 h) *via* the Ti-H<sub>2</sub>O<sub>2</sub> interactions.<sup>93</sup> TTIP or TiCl<sub>4</sub> present in aqueous solution produced >10 nm sized TiO<sub>2</sub> nano-sol. The chemical reaction yields a stable TiOCl<sub>2</sub> intermediate phase and anatase or rutile crystalline TiO<sub>2</sub> using TiCl<sub>4</sub>. The pH-controlled aqueous solution produced small anatase nano TiO<sub>2</sub>, which was unable to disperse in a few solutions. It may be because of the accumulation of the TiO<sub>2</sub> primary nanoparticles. Another reason for such case may be due to gradual precipitation by ageing at ambient conditions.<sup>94</sup> TiO<sub>2</sub> NPs were produced by means of a modified non-hydrolytic sol-gel technique at ambient conditions with TiCl<sub>4</sub> as the Ti-precursor at 85 °C.

The modified sol-gel method produced nano-TiO<sub>2</sub> of 2 to 10 nm size at 50–100 °C.<sup>75,79,95,96</sup> Hydrolyzed tetra-butyl titanate by diethyl ether synthesized highly crystalline anatase TiO<sub>2</sub> nanoparticles at 100 °C.<sup>97</sup> This method does not require additives, special equipment or template agents, which made it popular. Ethylene glycol-controlled condensation rates and hydrolysis at low temperature produced highly crystalline anatase nano TiO<sub>2</sub> (2–4 nm).<sup>98</sup> The scale-up of this novel method is possible due to the simple and reproducible route. Furthermore, *tert*-butyl alcohol was used to produce extremely soluble and superb dispersity anatase NPs (~3 nm) from TiCl<sub>4</sub> at 60 °C.<sup>73</sup> Various researchers demonstrated the effect of different solvents (ethanol, *n*-butanol, and hexanol) at various temperatures (90–170 °C) to yield TiO<sub>2</sub> NPs (3–5 nm).<sup>99</sup> Another sol-gel preparation of TiO<sub>2</sub> nanoparticles gives transparent suspensions due to less particle sizes of sub-5 nm.<sup>49</sup>

Recently, crystalline, phase-oriented nanostructured titania with different particle sizes at sub-zero temperatures (–196 °C and –10 °C) has been reported by Shejale *et al.*<sup>19</sup> The phase conversion between anatase and rutile was achieved by one-step chemical reaction involving titanium tetra-isopropoxide and ethyl alcohol. The synthesized TiO<sub>2</sub> nanocrystals displayed oval and nanorod morphologies by temperature variation. Interestingly, this method was further used to prepare TiO<sub>2</sub> up to –196 °C synthesis temperature (see Fig. 3b).

Pre-synthesized crystalline TiO<sub>2</sub> (np-TiO<sub>2</sub>) was used to develop TiO<sub>2</sub> ETL at a low temperature of ~70 °C, where the diameter was controlled *via* modulating solvent.<sup>100</sup> A low cost, short time, simple and minimal equipment process was proposed for developing TiO<sub>2</sub> NPs using the sol-gel method at ambient temperature. A homogenous sol was created as a forerunner in an organic setting by a varied combination of metal alkoxide by condensation and hydrolysis reactions. A wet algogel was obtained from the sol subsequently dried through a polymerization at ambient temperature, and multiple recrystallizations produced titania NPs (monodisperse and spherical) at lower temperature. These NPs were stable and highly pure.<sup>101</sup> Furthermore, diverse concentrations of titanium sulfate (Ti(SO<sub>4</sub>)<sub>2</sub>) solution was heated at different temperatures

(80, 90, and 100 °C) for 5 h to yield the precipitate. The preparation method decides the optimum temperature and concentration of Ti(SO<sub>4</sub>)<sub>2</sub>. After the hydrolysis, the mixture was strained with DI water to neutral and the precipitate was dried at 100 °C for 2 h.<sup>50</sup> A recent case demonstrated the synthesis of TiO<sub>2</sub> nanocrystals in the intermediate phase of amorphous and anatase *via* peroxo sol-gel method by simple and low temperature.<sup>96</sup>

## 2.2 Hydrothermal

Another versatile synthesis technique is the hydrothermal method, and is proved to be very significant to synthesize materials in aqueous solution by employing high temperature and high vapor pressure. The reaction is usually conducted using a steel pressure vessel known as an autoclave. The reaction inside the hydrothermal reactor as a closed system is still not clear.<sup>102</sup> Recently, the graphene oxide property to align with flow with the resin (thermoset) fixation effect was explored to see inside this mysterious black box (hydrothermal reactor). Fig. 4a throws light on the annular distribution of assembled-GO and axisymmetric poloidal structure, and inferred the annular convection. The temperature distribution and geometric symmetry of the reactant and their relation to the viscosity and reactors parameters have been studied.<sup>103</sup> Although it is a high temperature synthesizing process, many researchers reported the synthesis of titania at lower temperatures (see Fig. 4b). Zhang *et al.* reported the hydrothermal synthesis of large scale TiO<sub>2</sub> microspheres at relatively low temperature of 90 °C using aqueous Ti(SO<sub>4</sub>)<sub>2</sub> and urea as an additive/coordinating agent.<sup>12</sup> A low yield of TiO<sub>2</sub> crystal was obtained in the absence of urea. Here, the urea changes the coordination structure of TiO<sub>2</sub>, inducing heterogeneous nucleation of TiO<sub>2</sub>. Bu *et al.* synthesized TiO<sub>2</sub> using HNO<sub>3</sub> under hydrothermal conditions, and obtained a single crystal nanorod by further treating with anatase TiO<sub>2</sub> at a temperature as low as 70 °C.<sup>74</sup> The latter was formed by the hydrolysis of TBT. However, when these are dispersed in nitric acid followed by hydrothermal synthesis using steel autoclaves,

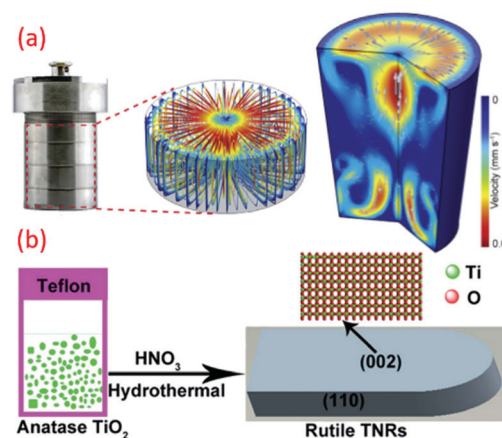


Fig. 4 (a) Photograph and simulated flow field inside the batch hydrothermal vessel (reproduced with permission.<sup>103</sup> Copyright 2020, Elsevier), and (b) schematic of low temperature synthesis of TiO<sub>2</sub> by hydrothermal technique (reproduced with permission.<sup>74</sup> Copyright 2015, Royal Society of Chemistry).



it resulted in well-defined titania nanorod architectures. Reports on the preparation of controllable crystalline  $\text{TiO}_2$  using micro-emulsion mediated hydrothermal method are also available.<sup>104</sup> Cellulose fabric nanocomposites consisting of  $\text{TiO}_2$  NPs, such as anatase, rutile and brookite, were produced by hydrothermal method (90 °C) by changing the HCl concentration. A strong ultrasonic processing of 30 min on fabric did not affect the  $\text{TiO}_2$  finished cellulose fabrics. These fabrics were conserved in the facile hydrothermal situations.<sup>52</sup>

### 2.3 Acid-assisted templating

The template-assisted method is another effective technique to fabricate nanomaterials, particularly of controlled size and shape. Well-ordered arrays of nano architecture materials can be easily fabricated by exploring such approach. For example, a low temperature template-assisted synthesis of a hierarchical mesoporous  $\text{TiO}_2$  nanowire bundle-like superstructure was reported by Jin *et al.*, which consisted of an amorphous surface and straight nanochannels. In another case, the triblock copolymer P123 was used as a mesoporous template at a low temperature (~80 °C) under acidic and wet conditions that resulted in a hybrid superstructure of amorphous and crystalline phases of  $\text{TiO}_2$  in the shape of  $\text{TiO}_2$  nanowire bundles. The obtained structure contains both anatase and rutile phase, and a lamellar mesophase is formed with the titanium precursor. The condensation reaction occurred due to the presence of ethanol and binding of P123 surfactant molecules with titania, which reduces hydrolysis. Similarly, three-dimensionally (3D) ordered meso-macroporous  $\text{TiO}_2$  samples with well-interconnected macropores, inner-particle mesopores, and a high specific surface area were reported by the same research group (see Fig. 5a).<sup>105,106</sup> In another study,  $\text{TiO}_2$  deposition was mediated by phosphonic acid through LPD on a titanium substrate. Hydroxyl groups were introduced on the surface of the Ti substrate by alkaline pre-treatment. This anchored phytic acid molecules and their self-assembly, and their several phosphate clusters would bring and consequently enable the  $\text{TiO}_2$  nucleation and progress at 50 to 80 °C, as shown in Fig. 5b.<sup>83</sup> The method has gained much attraction since it can fabricate 3D nanostructures of desired morphology and particle size in a well-controlled way.

### 2.4 RF sputtering

Generally, the sputtering technique consists of an ejection of atoms from a material, which is deposited on a substrate like a wafer or any other optical device with the help of high energy particles. This technique is recognized as a promising method for the production of large-scale uniform coatings with high packing density and strong adhesion to the substrate at relatively low temperatures. A low temperature growth study of nano-crystalline  $\text{TiO}_2$  thin films deposited by RF sputtering was reported by Safeen *et al.*, where they deposited  $\text{TiO}_2$  films using radio frequency (RF) sputtering in argon and argon-plasma at room temperature. The oxygen-to-metal ratio is one of the key parameters to achieve its stoichiometry and control oxygen vacancies defects (see Fig. 6).<sup>108</sup> The deposition procedure depends on the sputtering power, partial pressure of the gas

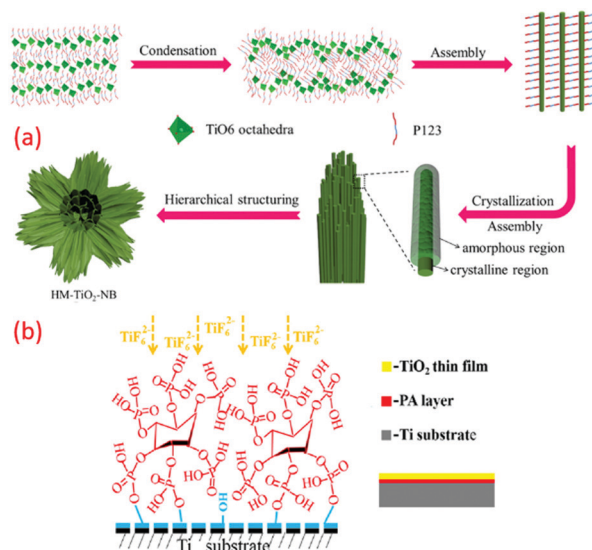


Fig. 5 (a) Mechanism of the categorized assemblies of the as-prepared HM- $\text{TiO}_2$ -NB structure; (a) the self-assembly of the hydrolysed titanium precursor molecules with the triblock copolymer P123 surfactant molecules to form a lamellar mesophase; (b) the formation of hybrid system surfactant- $\text{TiO}_2$  nanoparticles; (c) the formation of a 3D superstructure of surfactant nanowires; (d and e) the hierarchical structuration of bundles of mesoporous amorphous/crystalline  $\text{TiO}_2$  nanowires (reproduced with permission.<sup>107</sup> Copyright 2015, Elsevier) and (b) illustration of phytic acid layer template-assisted deposition of  $\text{TiO}_2$  film on titanium (reproduced with permission.<sup>83</sup> Copyright 2016, Elsevier).

used, and the total pressure. The technique holds specific advantages like high packing density and strong adhesion at relatively low temperatures. Deposition of anodized titanium foils (80 V for 10 min) and thin films (80 V for 55 s) on glass micro-scope slides using radiofrequency magnetron furnished self-organized  $\text{TiO}_2$  nanotubes at 25 °C.<sup>109</sup> Argon gas was used for sputtering  $\text{TiO}_2$  thin films over different substrates at room temperature. As for the rutile preparation, a piece of Cu (99.99%) rod with 1 mm width was placed symmetrically on target.<sup>59</sup> The thin films prepared by this technique has easy control for the preparation and its growth. Moreover, a very short time is required and has an advantage over the low-quality thin films prepared at high-temperature annealing and low-scale production involved in the traditional methods.

### 2.5 Pulsed laser deposition (PLD)

PLD is a physical vapor deposition (PVD) technique, which is comparatively simple. However, it is indeed a versatile experimental method that finds use as a patterning of very diverse range of materials in diverse areas of thin film deposition and also in multi-layer research.<sup>110</sup> Here, a high-power pulsed laser beam is focused inside a vacuum chamber to strike a target of the material that is to be deposited. The material is vaporized from the target in plasma, which deposits it as a thin film on suitable substrate. This process occurs in ultra-high vacuum or the presence of oxygen. This method was successfully used to deposit high quality metal oxide films especially  $\text{TiO}_2$  thin films. Ishii *et al.* prepared a single-phase rutile-type  $\text{TiO}_2$  thin



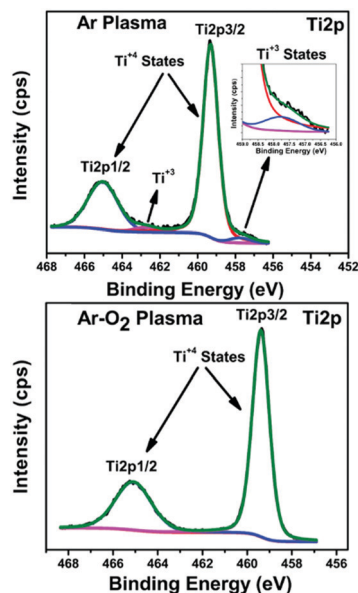


Fig. 6 XPS (Ti2p) of the TiO<sub>2</sub> films prepared in Ar and Ar-O<sub>2</sub> (20% O<sub>2</sub>) (reproduced with permission.<sup>108</sup> Copyright 2015, IOP Publishing, Ltd).

film by deposition under a vacuum at room temperature over a glass substrate.<sup>111</sup> Several scientific reports on doped TiO<sub>2</sub> nanocrystals were also reported by many authors using this technique.<sup>112</sup> PLD is considered as a relatively novel and distinctive method for producing many oxide thin films for energy device application owing to the flexibility, fast response, energetic evaporation and congruent evaporation properties. Another merit is its ability to function at relatively high pressures of reactive background gases, and also the ease of preparing many stoichiometric multi-component film depositions.

## 2.6 Dielectric barrier discharge (DBD) plasma

Recently, DBD was widely used for generating an atmospheric-pressure, non-thermal plasma, and was implemented successfully in the fabrication of TiO<sub>2</sub> nano powders, as well as thin films. Here, the discharge occurs within a gas gap between two electrodes using planar or cylindrical configurations.<sup>113</sup> However, the maximal thickness of the substrates is limited by the distance between the two electrodes. The coplanar DBD and surface DBD allow for using the desired thickness, and are promising for atmospheric-pressure low-temperature surface coatings. Di *et al.* fabricated atmospheric-pressure plasma CVD of TiO<sub>2</sub> films for the first time from TiCl<sub>4</sub> and O<sub>2</sub> using surface DBD technique, and deposited TiO<sub>2</sub> films were found to be an amorphous structure, as shown in Fig. 7a.<sup>114</sup> This method has gained much attention, and subsequently similar reports can be found within various literature (see Fig. 7b).<sup>113</sup> The mesoporous titania-conveying coatings were produced using wet-coating with a dispersal containing prefabricated titania NPs and a methyl-silica binder. Ink-jet printing was carried out for deposition of titania, subsequently mineralized at 70 °C and atmospheric pressure by diffuse coplanar surface barrier discharge (DCSBD) to get hybrid NC coating of titania and silica.<sup>81</sup>

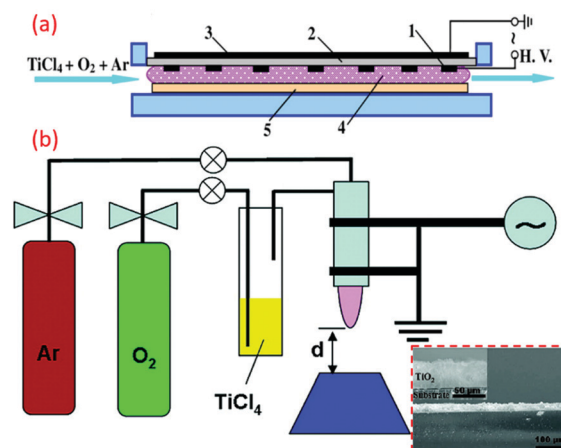


Fig. 7 (a) Schematic illustration of the device of the surface DBD-induced plasma CVD for the preparation of TiO<sub>2</sub> films (reproduced with permission.<sup>114</sup> Copyright 2009, IOP Publishing, Ltd) (b) DBD jet experimental setup for the TiO<sub>2</sub> film coating. (reproduced with permission.<sup>113</sup> Copyright 2010, American Chemical Society).

## 2.7 Electrophoretic deposition (EPD)

The EPD technique works on the principle of applying an electric field to collect charged nanoparticles at the oppositely charged electrode. Here, the progressive addition of charged nanoparticles results in the formation of thin films. Specifically, this technique is low temperature, low cost and versatile, which can be performed even at room temperature to synthesize various nanoparticles (see Fig. 8a). The facile setup allows for easy assimilation in the sector of industrial scale production of functional nanomaterials. Compared to other advanced shaping techniques, the EPD process is very versatile since it can be modified easily for a precise application. The deposition can be made on flat, cylindrical or any other shaped substrate with slight changes in the electrode design and positioning (see Fig. 8b).<sup>115,116</sup> EPD also offers effective control over the thickness and morphology of the deposited films through modifications in the deposition time and applied potential. Jouenne *et al.* successfully demonstrated the electrophoretic deposition at low voltage and concentration to yield uniform TiO<sub>2</sub> layers with a controllable thickness of 2.2 nm.<sup>41</sup> Similarly, many composite thin films of TiO<sub>2</sub> nanoparticles were deposited on different substrates using this technique.<sup>51</sup>

Anodic TiO<sub>2</sub> nanotubes were prepared by novel crystallization method at low temperature (70–90 °C). Although the mechanism of this method is not clear, it is popular due to the lower energy and simple equipment requirement compared to sintering. Various process parameters, such as solvents and treatment time, were studied systematically for low-temperature crystallization appliance of anodic TiO<sub>2</sub> nanotubes. TiO<sub>2</sub> nanocrystals are produced due to the low temperature crystallization observed by intense alteration of the surrounding water.<sup>117</sup> The morphology and crystallographic phase can be controlled by colloidal synthesis. This led to the electrophoretic deposition of colloidal TiO<sub>2</sub> rod-like shaped nanocrystals on a conductive substrate at 100 °C.<sup>51</sup> A novel template-free method was





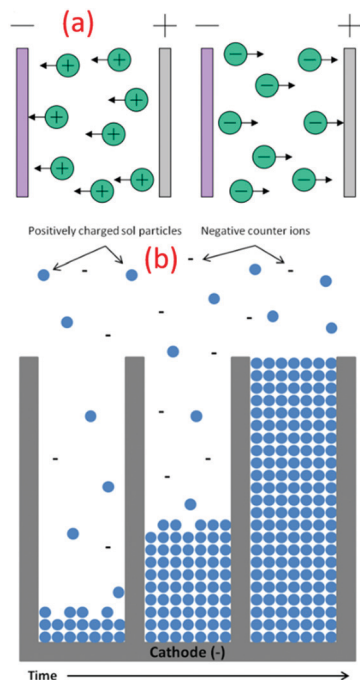


Fig. 8 (a) Schematic illustration of different types of electrophoretic deposition processes (reproduced with permission.<sup>115</sup> Copyright 2007, Elsevier). (b) Schematic of the nanorod growth process, demonstrating the electrophoretic motion of charged oxide particles into the pores of the template membrane, filling the pores from the bottom up with time (reproduced with permission.<sup>105</sup> Copyright 2004, Springer Nature).

developed to produce mesoporous films of nanocrystalline anatase  $\text{TiO}_2$  ( $\geq 80^\circ\text{C}$ ). These particles exhibited the great optical superiority beads that  $\text{TiO}_2$  affords.<sup>82</sup>

## 2.8 Solvo-thermal

Solvothermal synthesis is a method of producing chemical compounds, which is similar to the hydrothermal synthesis route.<sup>104</sup> Here, the synthesis is performed in a stainless-steel autoclave, and solvents other than water are usually employed.<sup>118</sup> The precise control over the morphology, size, distribution, and crystalline quality of several metal oxide nanoparticles can be successfully achieved by altering certain experimental conditions, such as the reaction temperature, reaction time, solvents, surface active agents, and precursor type.<sup>15</sup> This is owing to the preferential adsorption of solvent molecules or additives on certain surfaces of the products. Therefore, the growth of the surface is inhibited, resulting in the formation of products with unique morphologies. Thus, the formation of highly crystalline  $\text{TiO}_2$  nanocrystals of diverse morphologies is prepared *via* this technique at relatively low temperatures. Pookmanee *et al.* successfully synthesized  $\text{TiO}_2$  nanopowders by the low temperature solvo-thermal method with starting chemicals containing titanium isopropoxide, ammonium hydroxide and nitric acid in ethanol at  $100\text{--}200^\circ\text{C}$  for 2–6 h and maintaining pH as 1.<sup>60</sup> Nam *et al.* synthesized  $\text{TiO}_2$  using various ketone solvents, and its effects on the morphology and the structure were studied.<sup>119</sup> As the ketone solvents have low boiling points, the reaction was conducted at

temperatures much lower than  $100^\circ\text{C}$ . This method offers exact control over the particle size and morphology distribution by adjusting the different reaction parameters, such as temperature, time, and the solvent used. It is widely used as a facile one-step synthetic approach to many energy materials.

## 2.9 Phosphorus dendrimer approach

The phosphorus dendrimer approach technique is a new supra-molecular synthetic approach using phosphorous-containing dendrimer macromolecules made of well-defined branching units originating from a central core.<sup>120</sup> These are considered as materials, and can also be used as an intrinsic constituent of a material or as a modifier of the surface of a particular material. Brahmi *et al.* explored the surface-reactive fourth-generation phosphorus-dendrimers as molds to control the nucleation and growth of the titanium-oxo-species during the sol-gel mineralization process (see Fig. 9).<sup>71</sup> The dendritic medium provides low temperature for the formation of discrete anatase  $\text{TiO}_2$  nanocrystals of less than 6 nm, and it also prevented micro-phase separation, thereby providing well-defined hydrolysable sol-gel building blocks for further nucleation and growth of titanium oxide clusters. Velasco-Arias *et al.* synthesized anatase  $\text{TiO}_2$  nanoparticles (NPs) of sizes as low as 3 nm by a fast, inexpensive, one-pot procedure in dimethyl sulfoxide colloidal dispersions.<sup>121</sup>

Researchers showed that reactive sites are responsible for nucleation and growth, and ultimately different patterns. The inadequately coordinating surface in GO *versus* sturdy chelating locations for PGOI was demonstrated. PGOI- $\text{TiO}_2$  may possess more stability and homogeneity due to the higher stability of P-O-Ti bridges compared to GO- $\text{TiO}_2$ . The one-pot sol-gel method was carried out for the preparation of nanoparticles of GO- $\text{TiO}_2$  and PGOI- $\text{TiO}_2$  by means of a titanium source  $(\text{Ti}(\text{acac})_2(\text{OiPr})_2)$  and support (GO or PGOI). The carbon surface got attached with metal-oxo-species due to the alkoxide groups. Subsequently, a clustered metal oxide grew on the graphene surface by hydrolysis and condensation.<sup>122</sup> Limited numbers of researchers tried to associate organic and inorganic phases in a sole nanostructured, open structure fused material. Catechol-terminated phosphorus dendrimers (DGN:  $n = 1\text{--}5$ ) were developed with 5 different approaches for titanium alkoxide mineralization.<sup>120</sup> Although dendrimers approach are useful for many highly specialized applications, the high poly-valency of higher-generation dendrimers requires a well-controlled, target-tailored regioselective chemical engineering protocol which is the main drawback. The structural evolution of the dendrimers, from simple, monofunctional molecules to complex, multifunctional compounds, is indistinguishably associated with constant progress in traditional synthetic methods and the development of novel synthetic tools.

## 2.10 Reflux approach

The aqueous solution-based reflux synthesis is potentially used for the green synthesis of many nanostructure materials including titania.<sup>123</sup> A mixture of reactants along with solvent is placed in a suitable round bottom flask connected to a water-cooling condenser. The reaction vessel is heated in order to boil



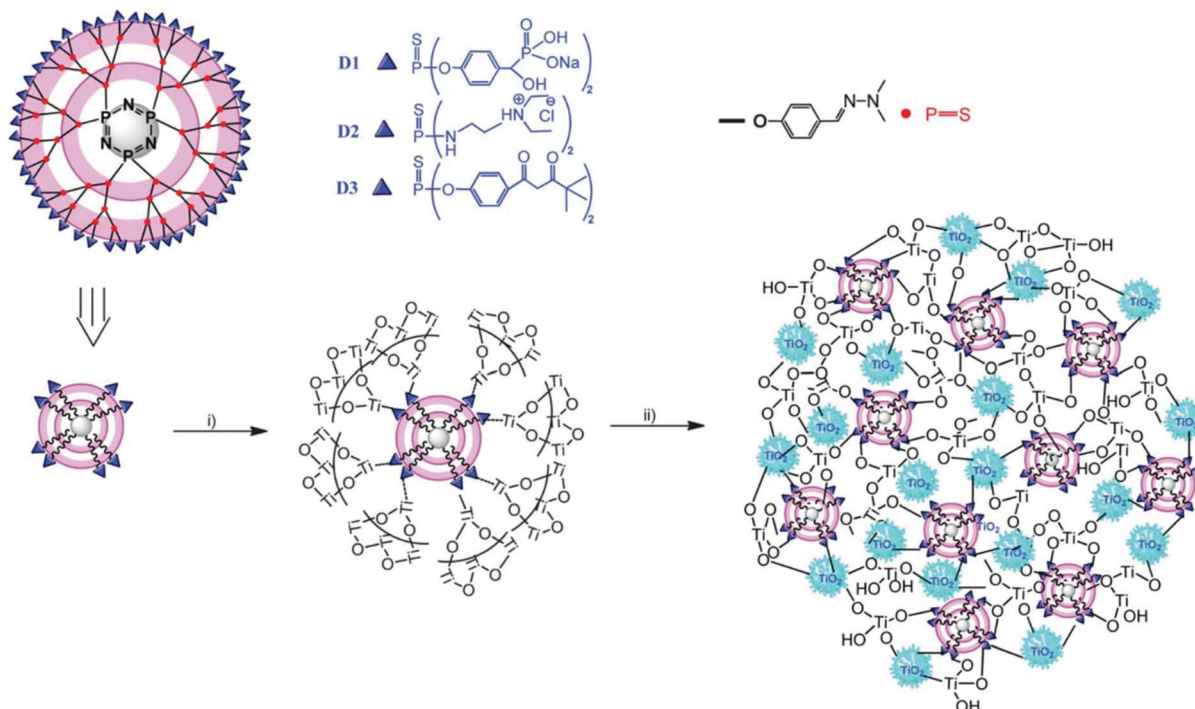


**Fig. 9** Representation of the structure of the fourth-generation phosphorus dendrimers (D1, D2 and D3) showing the cyclophosphazene core, the branches and the three chelating ligands (phosphonate, ammonium and acetylacetonate) located on the surface, and illustration of the MD<sub>x</sub> ( $x \frac{1}{4}$ , 2 or 3) preparation: (i) addition of Ti(OiPr)<sub>4</sub>, EtOH and H<sub>2</sub>O leads to hydrolysis–condensation of titanium alkoxide on the surface of the phosphorus dendrimers. (ii) Aging the material at 60 °C induces further condensation, growth and crystallisation of titanium dioxide. Small crystalline anatase nanoparticles (5 nm) are entangled within the hybrid material network (reproduced with permission.<sup>71</sup> Copyright 2013, Royal Society of Chemistry).

the reaction mixture. As a result, vapors produced from the mixture were condensed by the condenser, and then return to the vessel through gravity. By carefully controlling the various reaction parameters, such as the order of addition of precursors, the refluxing temperature, the refluxing time and cooling rate; the preferred morphology and crystalline phase of the nanostructures can be optimized. Ge *et al.* synthesized anatase TiO<sub>2</sub> thin films on glass substrates *via* a sol–gel method from refluxed sol (RS) containing anatase TiO<sub>2</sub> crystals at low temperature.<sup>124</sup> They carefully varied the refluxing time and the changes on the crystallinity, morphology and size of the RS sol were studied systematically. Xu *et al.* successfully synthesized F-doped TiO<sub>2</sub> under mild conditions, *i.e.*, at a temperature lower than 74 °C and ambient pressure by hydrolysis of titanium-*n*-butoxide in abundant NH<sub>4</sub>F–H<sub>2</sub>O acidic solution.<sup>125</sup> Anatase TiO<sub>2</sub> of high crystalline quality can also be prepared from microwave-assisted refluxing method at very low temperature, and also at very low power.

Simple precipitation at lower temperature by titanium sulphate without calcination produced mesoporous rutile TiO<sub>2</sub> NPs.<sup>91</sup> Reduced titanium dioxide (TiO<sub>2–x</sub>) was prepared by simple ethanol refluxing treatment (120 °C) with improved VIS photocatalytic properties with a higher density of Ti(III) species. Two optical features were observed in this case, a broad absorption band and sub-gap absorption tail. The first optical feature is responsible for the blue color, while the other is responsible for the band gap energy. Surface and subsurface

oxygen (O) vacancies are formed due to ethanol reflux treatment.<sup>123</sup> Even though the refluxing method is commonly used for metal oxide preparations, careful control over the size and morphology of the particle is very difficult due to the bumping (superheating) problems associated with this synthesis approach.

## 2.11 LTDRP-Low temperature dissolution-reprecipitation

Yin *et al.* synthesized rutile phase TiO<sub>2</sub> nano by a “low temperature dissolution–reprecipitation process” in liquid media.<sup>84</sup> Their study involved the crystallization of an amorphous precursor that could proceed at around room temperature, which was much lower than those of conventional calcination and hydrothermal reactions.<sup>72</sup> The thermodynamically stable rutile formed at low temperature below 70 °C. At higher temperature, metastable anatase crystals were obtained. Significant changes in the morphology, phase composition, microstructure and also the specific surface area of TiO<sub>2</sub> were varied depending on the reprecipitation temperatures.<sup>66</sup> Different morphologies, such as needle-like rutile titania and spherical anatase titania crystals with promising high specific surface areas, were obtained by this method. Fischer *et al.* reported a direct synthesis of non-agglomerated TiO<sub>2</sub> nanoparticles with diverse crystal phase ratios *via* LTDRP approach on a porous microfiltration membrane (polyethersulfone).<sup>126</sup> The variation in the amount of hydrochloric acid as well as the temperature between 0.1–1 M and 25–130 °C

with constant concentration of titanium precursor (titanium(IV) isopropoxide) resulted in high crystalline TiO<sub>2</sub> NCs.

## 2.12 Heterogeneous nucleation

Heterogeneous nucleation is a surface-assisted nucleation process and, in this process, the extent to which the surface can catalyze the nucleation depends on the contact angle of the nucleus with respect to the substrate selected. Direct deposition of supersaturated solutions of titania with complex shapes through heterogeneous nucleation is momentous as organic fibers. For example, paper and cotton have been successfully coated with small particles of TiO<sub>2</sub> and can be used for various self-cleaning fabric preparations. Imai *et al.* synthesized mono-disperse hollow nanocylinders of anatase crystalline titania particles from aqueous solutions of titanium tetra fluoride using alumina porous membranes as heterogeneous nucleation templates.<sup>73</sup> The prepared TiO<sub>2</sub> nanocylinders contain straight channels with mesoscale pores. Wang *et al.* explored this method and fabricated nano-TiO<sub>2</sub>/glass beads (GB) composite particles with a core/shell structure at temperature as low as 80 °C.<sup>76</sup> Qi *et al.* modified the method and successfully prepared a phase-pure rutile TiO<sub>2</sub> aqueous sol of 20 nm by heterogeneous nucleation using aqueous peroxotitanate solution and SnCl<sub>2</sub> as rutile-phase crystalline growth promoter at a temperature as low as 100 °C in one-step process.<sup>127</sup> Nucleation time determines the density and morphology of nano TiO<sub>2</sub> due to the linear relation of the substrate surface and nucleation during the process of liquid phase deposition (LPD). At a temperature of 50 °C during LPD, controlled structures of TiO<sub>2</sub> were obtained by controlling the nucleation time.<sup>128</sup>

## 2.13 Ionic liquids-assisted TiO<sub>2</sub> synthesis

Ionic liquids (ILs) are a special type of molten organic salts comprising distinct anions.<sup>129</sup> The properties of ILs can be easily tuned through the proper selection of the constituent cations and anions. Furthermore, the melting point of these ILs (below 100 °C) often falls below the reaction conditions, making these good candidates for many chemical syntheses.<sup>130</sup> Owing to their unique properties like negligible vapor pressure, thermal stability, and remarkable ionic conductivity and dissolution properties, they are considered as the green solvent, which is the potential replacement for many commonly used organic solvents. The ILs with some chosen specific properties are successively demonstrated to synthesize a variety of novel TiO<sub>2</sub> nanostructures with anticipated morphologies and functions.<sup>131</sup> The first report on low reaction temperature anatase TiO<sub>2</sub> nanosponges using the IL was reported by the Antonietti group.<sup>132</sup> Using 1-butyl-3-methylimidazoliumtetrafluoroborate, [C<sub>4</sub>mim]<sup>+</sup> BF<sub>4</sub><sup>−</sup> as a solvent, very fine crystalline anatase titania nanocrystals of 2–3 nm were synthesized at a temperature as low as 80 °C. The ILs used in this synthesis cause certain polymorph formations by restrictive crystal growth. Furthermore, a room temperature single-step interfacial sol-gel synthesis of hollow TiO<sub>2</sub> gel microspheres in the ionic liquid were reported by Nakashima *et al.*<sup>133</sup> In this study, titanium tetrabutoxide was dissolved in anhydrous toluene and

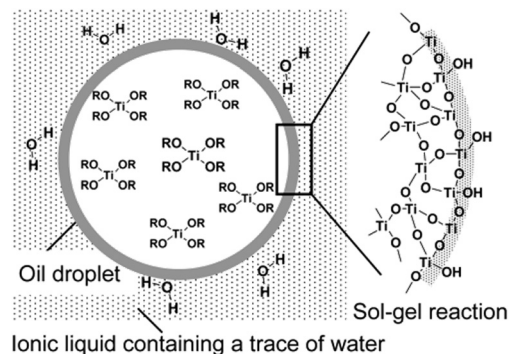


Fig. 10 Schematic Illustration of hollow TiO<sub>2</sub> microsphere formation by oil droplet/C<sub>4</sub>mim interface (reproduced with permission.<sup>133</sup> Copyright 2003, American Chemical Society).

injected into 1-butyl-3-methylimidazolium hexafluorophosphate ([C<sub>4</sub>mim]PF<sub>6</sub>) under vigorous stirring to get hollow titania microspheres (see Fig. 10). Calcination of the obtained gel microspheres resulted in the formation of hollow anatase TiO<sub>2</sub> microspheres. These microspheres can also be modified with metal nanoparticles or functional organic molecules to design different smart functional organic/inorganic hollow capsules. Various reports on the introduction of ILs during the synthesis route and the enhancement in the visible-light response of TiO<sub>2</sub> by doping with nonmetal elements constituting ILs (C, F, P, B), direct sensitization of TiO<sub>2</sub>, surface complex charge transfer, preferring oxygen vacancies and Ti<sup>3+</sup> species formation, and affecting the transport properties of photo-generated charges can be found.<sup>131,134–137</sup>

## 2.14 Microwave-assisted TiO<sub>2</sub> synthesis

Microwave (MW)-assisted synthesis method is a promising green chemistry approach to fabricate various nanomaterials and nanocomposites. This method provides homogenous heating to the reaction mixture to lessen the thermal gradients in the reaction mixture.<sup>138</sup> Several characteristics of microwave heating involve greener syntheses, less reaction time, negligible energy consumption, high reproducibility, and higher product yield with high purity.<sup>139</sup> Additionally, this technology can be combined with other green chemistry approaches such as ionic liquids, solvent-free reactions, and nontoxic precursors to make it more effective and energy-efficient. By this technique, the development of high-quality nanostructured TiO<sub>2</sub> with desired morphology can be synthesized without requiring any structure-directing agents. Low-temperature anatase titania nanowires were synthesized by Chung *et al.* using a microwave-assisted hydrothermal method.<sup>140</sup> The MW power of 350 W resulted in the formation of nanowires with a diameter of 80–150 nm. TiO<sub>2</sub> nanoparticles with suitable sizes and morphologies have been synthesized *via* MW methods for various energy conversion and storage devices.<sup>141–143</sup> The anatase titania nanostructures of size ~7 nm and ~100–400 nm were synthesized successfully from the thiobenzoate complex of titanium in benzyl alcohol and ethanol. The transparent and scattering nanoparticles of anatase TiO<sub>2</sub> obtained were successfully used as a photoanode in





solar cells application.<sup>144</sup> Various types of TiO<sub>2</sub> nanostructures, such as mesoporous anatase TiO<sub>2</sub>, nanocrystallite aggregates, porous anatase TiO<sub>2</sub> spheres, were applied to various energy conversion and storage devices.<sup>145–147</sup>

### 2.15 Ultrasonication synthesis

The sonochemical synthesis technique is very effective for fabricating novel nanostructured materials with unique properties, and is proved as an eco-friendly process. The deployment of an ultrasound of high intensity can provide a simplistic, adaptable synthetic tool for nanostructured materials.<sup>148</sup> The chemical effects of ultrasound do not come from direct interaction with molecular species, and instead come from the hot spots created during acoustic cavitation (the formation, growth, and implosive collapse of bubbles). They can be categorized as primary sonochemistry (gas-phase chemistry occurring inside collapsing bubbles), secondary sonochemistry (solution-phase chemistry occurring outside the bubbles), and physical modifications (caused by high-speed jets or shock waves derived from bubble collapse).<sup>149</sup> Thus, this technique allows for major control of the crystalline structure, size, and morphology of particles. Distinct topographies of the nanosized structures obtained *via* the sol-gel route can be endorsed by the use of ultrasonic irradiation during the hydrolysis step.<sup>148</sup> Furthermore, nanostructured metals, alloys, oxides, carbides and sulfides, nanometer colloids, and nanostructured supported catalysts can be prepared by this general route.<sup>150</sup> The sonochemical method has been demonstrated to fabricate various TiO<sub>2</sub> nanoarchitectures for various energy device applications.<sup>151–153</sup>

### 2.16 Nonaqueous solution synthesis

Nonaqueous solution routes to synthesize TiO<sub>2</sub> NPs are a potential alternative to the well-recognized aqueous sol-gel processes. This route bids advantages, such as high crystallinity at low temperatures, robust synthesis parameters, and the ability to control crystal growth without using surfactants.<sup>154</sup> The usage of organic solvents is the best alternative to aqueous chemistry to develop an efficient and transparent TiO<sub>2</sub> nanoparticles. The synthesis can be achieved by utilizing surfactants like tetra ethoxy silane and its substituents and other organic solvents. Benzyl alcohol, 2-butanone, xylene, dichloromethane, and others are some of the solvents already reported to synthesize titania nanoparticles (see Fig. 11).<sup>107,155,156</sup> High-quality titania NPs were prepared *via* a nonaqueous sol-gel route at low temperatures. TiCl<sub>4</sub> was added to anhydrous benzyl alcohol under vigorous stirring at room temperature as low as 40 °C.<sup>157</sup> Sofia Sandhu *et al.* reported a new deep eutectic solvent (DES), which acts as a templating and structure-directing agent used in hydrothermal synthesis to obtain nanosized titania. TiO<sub>2</sub> with well-defined morphology, reduced particle size, high surface area, and porosity can be achieved.<sup>158</sup> This method has gained attention due to toxic HF and ammonia capping agents in traditional synthesis protocols.

Another interesting study on controlled growth of anatase TiO<sub>2</sub> nanorods with high aspect ratio was reported by Cozzoli *et al.* by the hydrolysis of the titanium tetra-isopropoxide (TTIP)

### S<sub>N</sub>1 Reaction-assisted synthesis of oxides

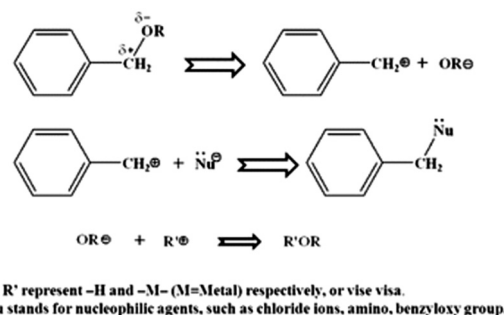


Fig. 11 Representation of the metal oxide nanoparticle synthesis and S<sub>N</sub>1 reaction mechanism of benzyl alcohol and metal chlorides (reproduced with permission.<sup>107</sup> Copyright 2013, Royal Society of Chemistry).

precursor in the presence of oleic acid (OLEA) as a surface directing agent at a temperature as low as 80 °C.<sup>77</sup> The latter work claimed that the unidirectional growth of TiO<sub>2</sub> nanorods resulted from the anisotropic reactivity of the titanium precursor. Furthermore, due to the chelating property of the surfactant OLEA, it is capable of suppressing the crystal growth along certain crystallographic orientations and the effective control of hydrolysis by regulating the water supply. Fast hydrolysis of the titanium precursor would result in rod-like structures. Slowing down the hydrolysis of precursors and promoting polycondensation, different crystalline structures of TiO<sub>2</sub> can be prepared in the desired shape. Hague *et al.* also studied the preparation of amorphous and crystalline TiO<sub>2</sub> using tetrabutyl titanate (TBT) as a titanium precursor by merely changing the washing solvent.<sup>159</sup> It was revealed that washing TiO<sub>2</sub> particles with water developed the crystalline TiO<sub>2</sub>, while washing the same particles with ethanol produced amorphous TiO<sub>2</sub>. Similarly, anatase-brookite TiO<sub>2</sub> polymorphs were also reported by a modified sol-gel method through careful control of the pH, *viz.*, 2, 4, 7 and 9.<sup>58</sup>

## 3. TiO<sub>2</sub> at low temperature

At a lower temperature preparation of TiO<sub>2</sub>, the process of nucleation and its rate significantly determine the phase, density and morphology of TiO<sub>2</sub>. Moreover, the thermodynamic stability of the individual phases of TiO<sub>2</sub> plays a crucial role during these formations. The surrounding temperature has a profound effect on the small crystal nuclei TiO<sub>2</sub> structure, which derived the final morphology and structure of TiO<sub>2</sub>. The phase and morphology of these crystals are also governed by the anions and solvents, which are a function of the temperature gradient. The absence of the higher temperature specifically induces a higher degree of the defects over the grain boundaries during the synthesis process and reduces the nanocrystalline particle growth. It has been observed that the gain in the anatase phase percentage is derived by the enhancement in the defects at the grain boundary with lower temperature and simultaneous corresponding lattice strain enhancement accelerate the grain growth. Such factors have



been studied by the pseudo-Voigt function, Rietveld refinement, Williamson–Hall (W–H) and Warren–Averbach functions. At lower synthesis temperature, the  $\text{TiO}_6$  octahedral unit arrangements during  $\text{TiO}_2$  formation result in the specific phase, size and shape formation. As shown in Fig. 12a, anatase (zigzag packing), *cis*-coordination, and rutile (linear packing) *trans*-coordination sites of octahedra are utilized for  $\text{TiO}_2$  crystal growth. The thermal gradient, specifically at high temperature in lower temperature conditions, tends to form a  $\text{TiO}_6$  octahedral unit closest linear packing. As shown in Fig. 12a, at  $-10^\circ\text{C}$  (at high temperature in lower temperature condition), the nucleation rate of the linearly packed  $\text{TiO}_6$  octahedral units is relatively slower than the growth rate, which has a tendency to form rod-shaped rutile crystals exhibiting less strain over the grain boundaries. Whereas at  $-40^\circ\text{C}$  (at low temperature in lower temperature condition), a high growth rate has occurred with simultaneously high fast nucleation, which promotes high defect and strain over grain boundaries and formed oval-shaped anatase crystals.<sup>2,19</sup> Different sizes of nano  $\text{TiO}_2$ , such as quantum, nano and bulk scale, possess different properties. Electron transfer pathways, light guiding, and reactant diffusion are controlled in a better way in the case of  $<100\text{ nm}$   $\text{TiO}_2$  nanoparticles. These functionalities are important in modified biological, physical and chemical properties.<sup>45,98</sup> Critical length scales of physical phenomena, such as charge transport distances and light absorption depth, the mean free path of electrons and phonons, or the Bohr exciton radius, are comparable to nanosized  $\text{TiO}_2$ . Many researchers demonstrated low-temperature  $\text{TiO}_2$  nanomaterials, and the related key parameters are summarized in Table 2.

The nature and property of the ultimate nanoparticle after a synthesis process, such as stability, morphology and particle size distribution, are governed by certain mechanisms of nucleation and growth. Among the various mechanisms reported, two popular mechanisms based on the kinetic model are mentioned below. The model proposed by Rivallin *et al.*

follows a two-step process rapid hydrolysis of the precursor, which condenses to form bigger particles.<sup>162,163</sup> This step is followed by an irreversible condensation process. Accordingly, this model defines the initial size and the growth size of the nanoparticles. However, it fails to discuss the final size of the nanoparticle. The second model proposed by Rempel and co-workers suggests that during the hydrolysis of precursors, the nuclei (primary particles) formation occurs.<sup>164</sup> This is followed by a period of reversible growth, whereby the growing process occurs due to attachment of the primary particles in a step-by-step fashion. Growth increases as the rate of attachment of the primary particles increases, which decreases the number of nuclei. Furthermore, there are five defined kinetic stages as defined by this model. However, this model does not describe a continuous equation for defining the size evolution of the particles in a broad range.<sup>165</sup> Forgacs *et al.* presented a universal model with three irreversible steps. In this, the authors envisaged a primary particle of  $\text{TiO}_2$  having a well-defined size formed by rapid hydrolyzing of the precursor. Dimerization and growth occur by the addition of the single unit particles to larger nanoparticles *via* attachments of the primary particle. The study showed that the experimental data is in accordance with a simple continuous function, which is used to understand the average particle size within a few hundred nanometers. Additionally, the studied model was successfully demonstrated in non-aqueous solvents for other nanoparticle systems, such as Zr-oxo-alkoxy.

Nanostructure building units are divided into 0D–3D structures depending on the size range. A dimension of  $<100\text{ nm}$  is possessed by 0D structures. Geometry-based nanofibers (NFs), nanorods (NRs), nanobelts (NBs), nanotubes (NTs), and nanowires (NWs) form 1D nanostructures.<sup>35</sup> 2D nanostructures comprise nanosheets (NSSs), nanonetwork, and nanoplates. Hierarchical and interrelated structures like a sphere, cube, or a matrix of other dimensions form 3D nanostructures.<sup>106</sup> Various properties of NPs depend on their dimensions and morphology. Better electronic or hole charge transport properties,

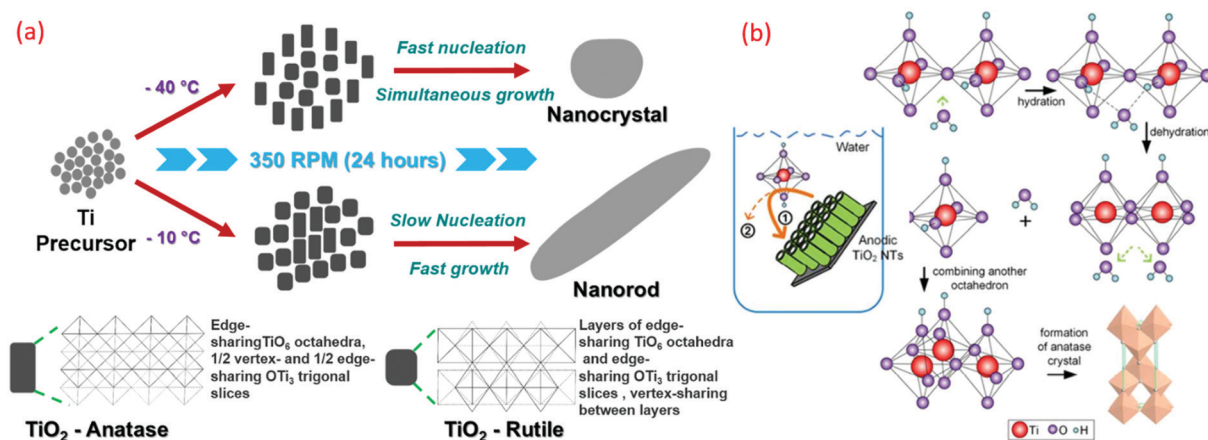


Fig. 12 Graphical representation of (a) A- $\text{TiO}_2$  and R- $\text{TiO}_2$  nanocrystal and nanorods synthesized by sol-gel method (reproduced with permission.<sup>2,8</sup> Copyright 2016, Royal Society of Chemistry). (b) Schematic illustration of hierarchical mesoporous  $\text{TiO}_2$  nanotubes, transformation of  $\text{TiO}_2$  from amorphous to anatase induced by water-assisted crystallization treatment process (reproduced with permission.<sup>117</sup> Copyright 2016, American Chemical Society).



**Table 2** A brief summary of the key development of TiO<sub>2</sub> materials at low temperature (−196 to 100 °C). A, R, B and Br represent anatase, rutile, brookite and bronze, respectively

Temp. (°C)	Precursors (additives)	Titania polymorph	Surface area (m <sup>2</sup> g <sup>−1</sup> )	Crystal size (nm) (morphology)	Band gap (eV)	Application	Ref.
−196 to 0	Titanium(IV) isopropoxide (TTIP) (HNO <sub>3</sub> )	R + A	100–135	4 to 14 (Oval & rod)	2.92–3.04	Solar cells (DSSC) and water remediation	2 and 19
−5 to 95	TiOCl <sub>2</sub> , TiCl <sub>4</sub> (HCl)	A	—	7.1–58.4 (Nanocrystal)	—	Supercapacitor	96
4	Ti(OEt) <sub>4</sub> (HCl) (HNO <sub>3</sub> , CH <sub>3</sub> COOH, H <sub>3</sub> PO <sub>4</sub> , H <sub>2</sub> SO <sub>4</sub> )	182	A	3.3–6.3 (Nanocrystal)	—	photocatalytic activity (Rhodamine B dye)	56
15	Tetrabutyl titanate (TBT) (HNO <sub>3</sub> )	A, B	—	4–4.7 (Nanocrystal)	3.04–3.19	Photocatalytic activity	160
25 to 100	TTIP (HCl)	R/A	106–212	4.8 to 5.2 (Needle-R & spherical A)	3.01–3.06	Photocatalytic activity	72
RT	TiCl <sub>4</sub> (ethanol, benzyl alcohol)	A	—	9.2–9.7 (Film)	—	Perovskite solar cells (PSCs)	161
RT-90	TTIP (HCl)	A, R, B	—	3.5–9.5 (Rod & flower)	—	photocatalytic activity (methylene blue)	126
40, 60, 80, 100	Ti(SO <sub>4</sub> ) <sub>2</sub> (H <sub>2</sub> SO <sub>4</sub> )	R	368	5 (Nanocrystal)	—	Adsorption (methylene blue)	91
50	TTIP (glacial acetic acid)	A	309	5.3 (NP chains)	—	DSSC	69
50, 60, 70, 80 & 90	TBT (acetic acid)	A	247–345	3.5 to 5.4 (Mesoporous crystals)	3.01–3.16	Photocatalytic activities	75
60	TTIP (phosphorus dendrimers)	A	230–240	4.8 to 5 (Small crystalline particles)	—	—	71
60	TiCl <sub>4</sub> (ethanol & water)	A	94.0–166.8	6.8 to 9.5 (Flower- or urchinlike)	3.05–3.19	Photocatalytic activities	70
60–80	TTIP (HNO <sub>3</sub> )	A	—	~5 (Nanocrystal)	—	PSCs	94
60–80	Ti Foil (H <sub>2</sub> O <sub>2</sub> )	A, R	—	10–20 (Nanorods, nano-wires, & nanoflowers)	—	Photodegradation (phenol)	93
70	TBT (HCl, HNO <sub>3</sub> )	R	—	20 to 50 (Single crystal nanorods)	2.95–3.0	Photocatalytic activities	74
70	TiCl <sub>4</sub> (CTAB, (NH <sub>4</sub> ) <sub>2</sub> SO <sub>4</sub> )	A, R	104–124	9.7–11.5 (Sphere-shaped)	3.3	Photo-electrochemical and catalytic activity	95
80	Tetrabutyl titanate (phytic acid, acetylacetone, ethanol)	A	0.26–12.17	10 to 50 (Core/shell)	—	Wear-resistance coatings	76
80	TiCl <sub>4</sub> (C <sub>16</sub> mimCl & C <sub>4</sub> mimBF)	Br	200	2.7 to 3.7 (Nanoparticles & nanofibers)	—	—	78
80	TTIP (HNO <sub>3</sub> )	A	135	15–20 (300–400) (Nano-aggregates)	—	Solar cells (DSSC)	90
100	TTIP (acetic acid)	A/B	—	2.7 to 7.9 (Irregularly shaped nanoparticles)	3.15–3.58	—	79

large specific surface area, high aspect ratio, and great transport properties of the electronic or hole charge are advantages of 1D NPs compared to other nanoparticles.<sup>36</sup> Various applications, such as catalytic, photovoltaic, gas sensors, detoxification, and energy storage, used 1D TiO<sub>2</sub> NPs for its advantages of unexceptionable surface activity and opportune electronic band structure.<sup>4</sup> The mechanism behind the few morphologies is illustrated in Fig. 12b.<sup>105</sup>

The morphological structure of a nanoparticle in general is governed by various factors involved during the synthesis process, such as the ratio of solvent: water, pH level, time, temperature and presence of any templates. This is highly important for use pertaining to specific applications, such as in medicine for drug delivery, sensors, and optoelectronics. Therefore, controlling the size, morphology, phase and surface-to-volume ratio of TiO<sub>2</sub> have significant wide range of applicability. Generally, the nanoparticles, especially TiO<sub>2</sub>, are prepared by means of the hydrolysis of the titania precursor in an acidic medium, followed by processes such as dehydration. Furthermore, to improve and control the morphology and size, modified synthesis strategies were adopted. For example, Matijević *et al.* hydrolyzed the TiCl<sub>4</sub> precursor to form

spherical 1–4 µm sized titania.<sup>166</sup> Similarly, the hydrolysis of the titanium precursor in an alcoholic medium can reduce the size of the spherical titania in a range from 300–700 nm.<sup>167,168</sup>

A general mechanism of synthesis is given by Pal *et al.* following a sol-gel synthesis process, whereby titanium glycolate is formed from the titanium butoxide precursor and ethylene glycol.<sup>68</sup> This is followed by slow hydrolysis in the presence of acetone and water to form spherical titania through a process of nucleation and growth by forming an intermediary metal alkoxide. The use of acetone accelerates the hydrolysis. However, the size is controlled by the amount of water. For example, it was observed that homogenous titania was formed when the water content of acetone was kept between 0.4% and 0.05%. An excess results in the formation of inhomogeneous titania, and the lack of water prevents the formation of titania altogether. The alkoxide group renders the intermediate metal alkoxide reactive and susceptible to nucleophiles. Therefore, in order to control the rapid process, bulky and branched groups such as butoxy are used. Furthermore, the use of chelating agents and chemical modifications with alcohols and pH are used to retard the hydrolysis and condensation rate to obtain smaller nanoparticles of titania. A similar scheme was also





given by Mahshid *et al.* of various processes of oxolation and ololation to form a polymerized network, leading to the formation of titania.<sup>169</sup> For the rate of hydrolysis, the pH level strongly rules the mechanism towards which the formation of the phase and structure of TiO<sub>2</sub> is governed. For synthesizing nanotubules, nanorods and nanowires of TiO<sub>2</sub>, a template (such as alumina and AAO templates) is used.<sup>170</sup> The template membrane is then immersed in the sol-gel titania precursors. Depending on the time and conditions, the diameters of the 2-D titania can vary.

### 3.1 0-Dimensional (0D)

A 0D nanoparticle refers to spheres with a diameter of <100 nm. The difficult and uncontrollable reaction process of the 0D TiO<sub>2</sub> preparation is a common issue. However, typical technologies of preparation are given in the following text.<sup>4</sup>

Controlled temperature (92–98 °C) and a higher amount of water (0.45 mL) produced oval shaped nanoparticles of pure TiO<sub>2</sub>(B). The presence of the BF<sub>4</sub> ion is essential for attaining the pure TiO<sub>2</sub>(B) phase.<sup>78</sup> Anatase (zigzag packing) and rutile (linear packing) demonstrates different structures due to a difference in the particle shape and size at sub-zero temperatures.<sup>58</sup> The *cis*-coordination and *trans*-coordination sites of the octahedral in anatase and rutile, respectively, are used for crystal growth (see Fig. 13a). A few researchers suggested that anions and solvents govern the phase and shape of nanoparticles of TiO<sub>2</sub>.<sup>99,119</sup> TiO<sub>6</sub> octahedral units form the closest linear packing at higher temperature. However, at 40 °C, the development takes place concurrently with fast nucleation, corresponding to the anatase

phase with a zigzag packed crystal assembly with high strain (0.0367) on the particle surface.<sup>2,19</sup>

Ti(SO<sub>4</sub>)<sub>2</sub> hydrolysis could get hampered due to the faster generation of TiO<sub>2</sub> precipitation, leading to a decrease in the yield of oval-shaped TiO<sub>2</sub>, as shown in Fig. 13b. The low temperature hydrolysis can be attained at 100 °C (boiling point of water), while the hydrolysis rate was very slow at lower temperature (80 °C) for commercial purposes.<sup>50</sup> The average diameter of the particle was obtained as 5 nm during the preparation of TiO<sub>2</sub> NPs at a temperature of 80 °C (see Fig. 13c).<sup>91</sup> TiO<sub>2</sub> structures (40–50 nm) were formed due to the agglomeration of smaller nanoparticles of 20–25 nm. A diffuse coplanar surface barrier discharge was used for coatings at atmospheric pressure and low temperature. This technique produced nanoparticles of 50–250 nm pore size, as shown in Fig. 13d.<sup>81</sup> TiO<sub>2</sub> quasi-monodispersed particles of 9.2 and 9.7 nm size were produced from TiCl<sub>4</sub>. The dropwise addition of TiCl<sub>4</sub> in cold anhydrous ethanol (2 mL) was carried out with vigorous stirring. Anhydrous benzyl alcohol (10 mL) was added to this solution after attaining room temperature with stirring (10 min). This solution was sealed and kept in an oil bath at 85 °C for 12 h without stirring. TiO<sub>2</sub> NPs were precipitated from this solution by adding diethyl ether (see Fig. 13e).<sup>161</sup> Sol-gel chemistry is used to get nano TiO<sub>2</sub> (<10 nm) using titanium alkoxide (TTIP or TiCl<sub>4</sub> aqueous solution). Anatase or rutile crystalline TiO<sub>2</sub> can be achieved using TiCl<sub>4</sub> with stable TiOCl<sub>2</sub> as an intermediate phase (see Fig. 13f).<sup>94</sup> An amorphous structure of TiO<sub>2</sub> with randomly distributed channels (10 nm) was found to be immersed among the disordered structures at 25 to 80 °C. As shown in Fig. 13g, a partially crystalline or amorphous material observable by low-density faint rings was demonstrated by selected area electron diffraction pattern (SAED) images.<sup>79</sup> DBD jet was used for the deposition of TiO<sub>2</sub> films (30 W RF power) using TiCl<sub>4</sub>/O<sub>2</sub> as precursors and argon as a plasma generation gas (see Fig. 13h).<sup>113</sup>

### 3.2 1-Dimensional (1D)

The peptization process (2–100 °C) parameters were maintained to get the rod shape TiO<sub>2</sub> in the presence of a base in aqueous medium by hydrolysis.<sup>64</sup> The hydrolysis catalyzed by trimethyl amino-*N*-oxide dihydrate (TMAO) in aqueous solution produced nanorods (diameter: 5 nm, length: 30–40 nm). Subsequently, the reaction flask was insulated for 5 days in an inert atmospheric condition and under stirring at 100 °C.<sup>51</sup> Titanium tetra-isopropoxide (TTIP) (H<sub>2</sub>O:TTIP molar ratio ranging from 40:1 to 150:1) was hydrolyzed by oleic acid (OLEA) at 80–100 °C to produce organic-capped anatase TiO<sub>2</sub> nanorods. A crystalline product was warranted during polycondensation using catalysts of tertiary amines or quaternary ammonium hydroxides (see Fig. 14b).<sup>77</sup> Concentrated HNO<sub>3</sub> was used to treat anatase TiO<sub>2</sub> in mild hydrothermal circumstances to acquire uniform TNRs with major active (002) facets of rutile TiO<sub>2</sub> (see Fig. 14f).<sup>74</sup> The titania powders crystallized by LTDRP in 0.5 M HCl solution at diverse temperatures. The needle-like rutile powders with an aspect ratio of 6 and 3.5 were obtained at 25 °C and 70 °C.<sup>66</sup> Dehydration and crystallization of dissolved Ti(OH)<sub>6</sub> formed anatase NTs and NCs. This

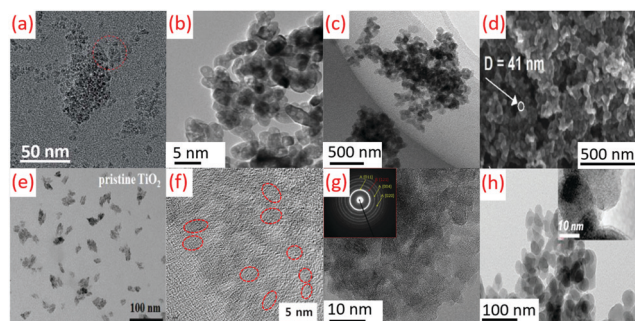


**Fig. 13** TEM images of (a) oval-shaped TiO<sub>2</sub> obtained at −40 °C by sol-gel method (reproduced with permission.<sup>2</sup> Copyright 2016, Royal Society of Chemistry), (b) TiO<sub>2</sub> obtained by hydrolysis at 80 °C (reproduced with permission.<sup>50</sup> Copyright 2015, Balaban Desalination Publications), (c) TiO<sub>2</sub> nanoparticles prepared at a reflux temperature of 80 °C (reproduced with permission.<sup>91</sup> Copyright 2017, Taylor & Francis), (d) TiO<sub>2</sub> prepared by air plasma at 70 °C (reproduced with permission.<sup>81</sup> Copyright 2016, American Chemical Society), (e) TiO<sub>2</sub> NPs synthesized by using a modified non-hydrolytic sol-gel method at 85 °C (reproduced with permission.<sup>161</sup> Copyright 2019, John Wiley and Sons), (f) TiO<sub>2</sub> nano-sol by sol-gel method at 60 °C (reproduced with permission.<sup>94</sup> Copyright 2019, Elsevier), (g) Anatase TiO<sub>2</sub> nanoparticles synthesized by an acid-assisted sol-gel method at 80 °C (reproduced with permission.<sup>79</sup> Copyright 2015, Elsevier), (h) TiO<sub>2</sub> films fabricated using atmospheric pressure dielectric barrier discharge jet at RT (reproduced with permission.<sup>113</sup> Copyright 2010, American Chemical Society).



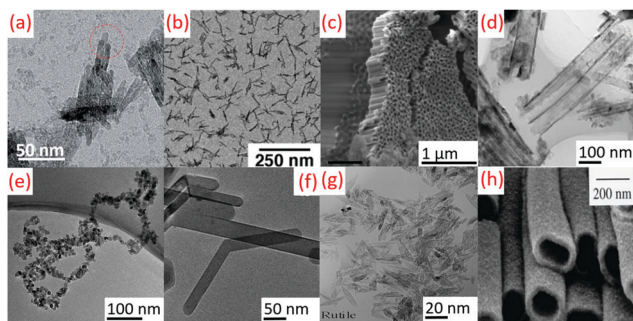


**Fig. 14** TEM images of (a) rod-shaped  $\text{TiO}_2$  prepared at  $-10^\circ\text{C}$  by sol-gel method (reproduced with permission.<sup>2</sup> Copyright 2016, Royal Society of Chemistry), (b)  $\text{TiO}_2$  nanorods synthesized by hydrolysis at  $80-100^\circ\text{C}$  (reproduced with permission.<sup>77</sup> Copyright 2003, American Chemical Society), (c) SEM images of nanotubes by anodizing titanium foil at room temperature (reproduced with permission,<sup>109</sup> Copyright 2018, Elsevier), TEM images of (d) anodic  $\text{TiO}_2$  NT arrays prepared by water-assisted crystallization treatment process at  $90^\circ\text{C}$  (reproduced with permission.<sup>117</sup> Copyright 2016, American Chemical Society), (e) anatase  $\text{TiO}_2$  nanoparticle chains by hydrolysis at  $50^\circ\text{C}$  (reproduced with permission.<sup>69</sup> Copyright 2015, Royal Society of Chemistry), (f) TEM images of  $\text{TiO}_2$  single crystal nanorods prepared by sol-gel and mild hydrothermal at  $343\text{ K}$  (reproduced with permission.<sup>74</sup> Copyright 2015, Royal Society of Chemistry), (g) rutile/anatase nanocrystals prepared by a low temperature dissolution-reprecipitation process at  $40-70^\circ\text{C}$  (reproduced with permission.<sup>84</sup> Copyright 2015, Chemical Society of Japan), (h) anatase  $\text{TiO}_2$  nanotubes in porous alumina membranes at  $60^\circ\text{C}$  (reproduced with permission.<sup>73</sup> Copyright 1999, Royal Society of Chemistry).

mechanism provided insights into the low temperature crystallization method (see Fig. 14d).<sup>117</sup> Uniform  $\text{TiO}_2$  nanotubes (diameter:  $130 \pm 8\text{ nm}$ , length:  $13 \pm 0.1\text{ nm}$ ) were formed using Ti foil anodization at room temperature,  $80\text{ V}$  and  $10\text{ min}$ , as shown in Fig. 14c.<sup>109</sup>

Aqueous solutions of titanium tetrafluoride were used to prepare anatase nanotubes with straight channels (diameter:  $50-150\text{ nm}$ ) at  $60^\circ\text{C}$  using alumina membranes. Nanotube walls had pores of  $10\text{ nm}$  size. The morphology was controllable due to no annealing (see Fig. 14h).<sup>73</sup> Cui *et al.* fabricated  $\text{TiO}_2$  nanochain structures with a large surface area much higher than the separated nanoparticles.<sup>69</sup> Another report on the low temperature  $\text{TiO}_2$  nanochains were found, but when applied in energy devices, showed a slower electron diffusion rate with longer electron lifetime.<sup>35</sup> The nano  $\text{TiO}_2$  chains were arranged by the hydrolysis of TTIP mixed with a large amount of glacial acetic acid (HAc) at  $50^\circ\text{C}$ . Acetic acid slowed down TTIP hydrolysis when water was introduced due to the lower hydrolyzable property compared to isopropoxy. The formed gel was stable and durable along with water-soluble titania, which was stable in the presence of HAc (see Fig. 14e).<sup>69</sup>

### 3.3 2 & 3 Dimensional (2D and 3D)

Jin *et al.* fabricated hierarchical mesoporous  $\text{TiO}_2$  nanowire bundles (HM- $\text{TiO}_2$ -NB) using a P123 surfactant copolymer by template-assisted method.<sup>105</sup> The condensation was aided by the surfactant, and was further promoted by hindering hydrolysis using HCl. During the process, the nanoparticles that were

aligned underwent condensation in the presence of the P123 and formed a 3D superstructure of nanowires. Owing to the low temperature used for the synthesis, the amorphous titania uniformly covered the outer layer of each nanowire. These nanowire structures can have further structuration in the forms of bundles that can yield straight nanochannels of uniform size, along with nanowires, as shown in Fig. 15c.

Wang *et al.* fabricated  $\text{TiO}_2$  flower-like superstructures using a simple low temperature sol-gel method.<sup>171</sup> SEM images confirmed the flower-like morphological structure with the collection of a large number of nanorods of length around  $15\text{ nm}$  with pointed ends. The interesting outcome of the reaction was when the molar ratios of the precursors ( $\text{TiCl}_4$  and ethanol) were doubled during the synthesis, and spherical urchin-like complex structures were obtained with a size of around  $500\text{ nm}$ .

Molar ratios of  $\text{TiCl}_4$ , ethanol and water were adjusted at  $50^\circ\text{C}$  to produce different rutile  $\text{TiO}_2$  NPs. The outcome of  $\text{H}^+$ ,  $\text{Cl}^-$ , and ethanol on the morphology of rutile nanorods were studied in detail, as shown in Fig. 15a.<sup>70</sup>

A high surface area of the rutile structure was observed after crystallization at room temperature in HCl or  $\text{HNO}_3$ . A very slow precipitation rate at  $60^\circ\text{C}$  can achieve stable and compact rutile nuclei, where metastable anatase was formed at a high reprecipitation rate and temperature (see Fig. 15d).<sup>66</sup> During the sol-gel method, a spherical-shaped structure is mainly governed by kinetic control rather than thermodynamics. By allowing the polymerization and delaying hydrolysis, effective control over the shape can be achieved. Cozzoli *et al.* achieved the suppression of anisotropic growth by the slow addition of water, which promoted the uniform growth of  $\text{TiO}_2$  nanocrystals in all directions, giving it a spherical shape.<sup>77</sup> Huang and others also observed the formation of spherical  $\text{TiO}_2$  crystals by the usual sol-gel method, but with short crystallization time.<sup>89</sup> They also observed the formation of large  $\text{TiO}_2$  spheres with extended reaction time.  $\text{Ti}(\text{SO}_4)_2$  aqueous solution ( $0.15\text{ mol L}^{-1}$ ) with urea

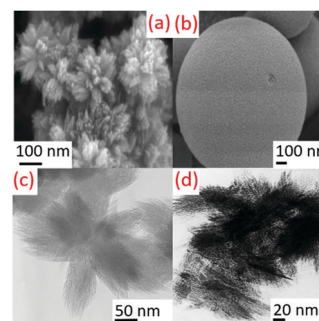


**Fig. 15** (a) Rutile  $\text{TiO}_2$  nanorod superstructures prepared by hydrolysis at  $50^\circ\text{C}$  (reproduced with permission.<sup>8,70</sup> Copyright 2007, American Chemical Society), (b) SEM image of  $\text{TiO}_2$  microsphere prepared by hydrothermal treatment at  $90^\circ\text{C}$  (reproduced with permission.<sup>12</sup> Copyright 2015, Taylor & Francis), (c) hierarchically mesoporous  $\text{TiO}_2$  nanowire bundles prepared at  $40-80^\circ\text{C}$  (reproduced with permission.<sup>107</sup> Copyright 2015, Elsevier), (d) nanosize rutile phase bundles prepared by low temperature dissolution-reprecipitation process at RT (reproduced with permission.<sup>66</sup> Copyright 2002, Elsevier).





(molar ratio urea/Ti 1/5) gave anatase TiO<sub>2</sub> microspheres at 90 °C through the hydrothermal reaction (see Fig. 15b).<sup>12</sup>

## 4. Analysis and characterizations

The morphology and grain size of TiO<sub>2</sub> NPs prepared at low temperature were usually checked by using a grain size of TiO<sub>2</sub> NPs (TEM and SEM). It demonstrated that high-resolution TEM (HRTEM) is one of the utmost dominant and resourceful methods to detect the crystal facets and shapes of TiO<sub>2</sub> NCs. Other complementary techniques such as EDXS and EELS enable the gaining of information on the chemical and electronic forms at the sub-nanometer scale with atomic resolution. Several properties of materials, such as the structural, charge carrier dynamics, and optoelectronics, can be characterized by TEM in TiO<sub>2</sub> nanostructures.<sup>49</sup>

### 4.1 Structural properties

XRD is crucial in the identification of the crystal assembly and the crystallinity, and in assessing the crystal grain size, according to the Scherrer formula. Crystal unit cells show a particular planar reflection, giving a diffraction pattern broadening of a particular peak in the XRD pattern. It is contrariwise related to the complete width at half-maximum (FWHM) of a distinct peak. It means that a decrease in the peak shows an increase in the crystalline size. XRD has a detection limit that restricts the accurate measurement of <3–4 nm nanoparticles, and so Raman spectroscopy is used for such samples.<sup>49</sup>

Anatase, brookite, and rutile TiO<sub>2</sub> give characteristic diffraction peaks at 25.3°, 14.2°, and 27.4°, respectively. The weight percentage of these different phases can be determined using XRD analysis (see Fig. 16a). The fractions of rutile and anatase in TiO<sub>2</sub> were estimated using the following equation  $WR = IR/(0.88IA + IR)$ , where WR is a percentage of rutile, and IR and IA are the diffraction intensities peak of rutile (110) and anatase (101), respectively.<sup>172</sup> Gaussian fitting of the XRD peaks furnished the magnitude of the IR and IA.<sup>173</sup>

Defective small particles on the amorphous grain boundary give broad diffraction peaks. These particles reduce the development of the NPs due to the strain on the boundaries.

Estimation of the lattice and size of NPs is usually estimated by the *pseudo-Voigt function*, *Rietveld refinement*, and *Warren-Averbach* analysis.<sup>174</sup> The strain and size-prompted broadening is checked by the simplified primary breadth technique Williamson–Hall (W–H) analysis by assessing the peak width corresponding to  $\theta$ .<sup>175</sup> The Williamson–Hall equation is expressed as:  $(\beta \cos \theta / \lambda) = (1/D) + \eta(\sin \theta / \lambda)$ , where  $\beta$  is the full-width half maximum (FWHM),  $\theta$  is half the diffraction angle of the diffraction peaks of rutile, anatase and rutile-anatase mixed phases, and  $\lambda$  is the wavelength of X-ray.  $D$  is the crystal size and  $\eta$  is the value of lattice strain. The linearly fitted  $X$  axis as  $\beta \cos \theta / \lambda$  and  $Y$  axis as  $\sin \theta / \lambda$  are plotted and the slope provided the effective lattice strain, as shown in Fig. 16c. The above the equation represents a uniform deformation model (UDM), and was used to estimate the crystal-line size.<sup>19</sup>

From comparing the irreducible representation of the light scattering modes with the crystal phase symmetry, the three phases of anatase, brookite, and rutile have 6(3E<sub>g</sub> + 2B<sub>1g</sub> + A<sub>1g</sub>), 36(9A<sub>1g</sub> + 9B<sub>1g</sub> + 9B<sub>2g</sub> + 9B<sub>3g</sub>), and 4(A<sub>1g</sub> + B<sub>1g</sub> + B<sub>2g</sub> + E<sub>g</sub>) Raman active modes, respectively. Brookite, either natural or synthetic, shows strong Raman peaks at 128 (A<sub>1g</sub>), 153 (A<sub>1g</sub>), 247 (A<sub>1g</sub>), 322 (B<sub>1g</sub>), 366 (B<sub>2g</sub>), and 636 (A<sub>1g</sub>) cm<sup>−1</sup>. Anatase exhibits characteristic Raman scattering at 146 (E<sub>g</sub>), 396 (B<sub>1g</sub>), 515 (A<sub>1g</sub>), and 641 (E<sub>g</sub>) cm<sup>−1</sup>, while rutile shows typical scattering at 143 (E<sub>g</sub>), 235 (two-phonon scattering), 447 (E<sub>g</sub>), and 612 (A<sub>1g</sub>) cm<sup>−1</sup>. Raman spectroscopy is efficiently used for phase identification and probing oxygen deficiency of matrix of TiO<sub>2</sub> (see Fig. 16b). An increase in oxygen vacancies led to increased and decreased wavenumbers of the anatase E<sub>g</sub> mode (146 cm<sup>−1</sup>) and rutile E<sub>g</sub> mode (447 cm<sup>−1</sup>), respectively.<sup>49</sup>

### 4.2 Surface and optoelectronic properties

The electronic conductivity of rutile TiO<sub>2</sub> is governed by Ti<sup>3+</sup> sites, which is related with oxygen vacancies and does not depend on ionic conduction.<sup>176</sup> Unsintered rutile powder and sintered rutile powder demonstrated the required activation energy as 1.75 and 1.7 eV, respectively, for the electronic conductivity. As the heating reduction in the vacuum controls the dielectric coefficient and effective electron mass of TiO<sub>2</sub>

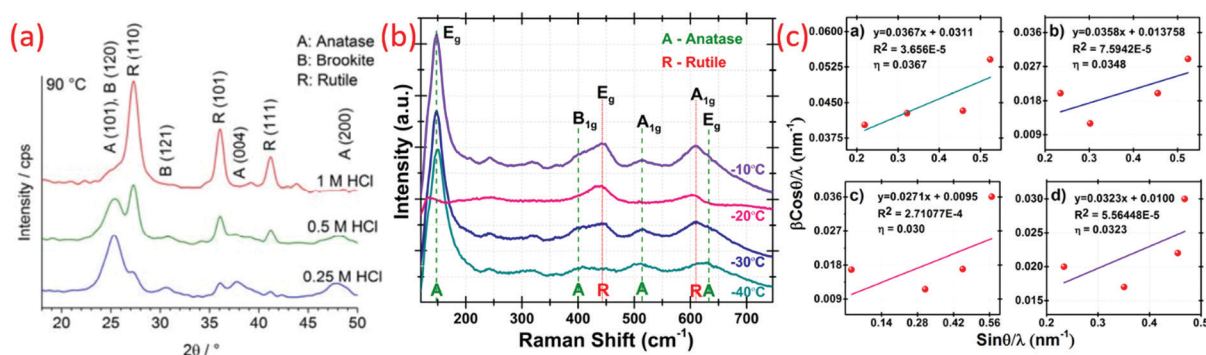


Fig. 16 (a) XRD pattern of TiO<sub>2</sub> prepared at 90 °C (reproduced with permission.<sup>8,126</sup> Copyright 2017, MDPI), (b) Raman spectra of anatase and rutile TiO<sub>2</sub> and (c) Williamson–Hall plot of nano-TiO<sub>2</sub> synthesized at low (sub-zero) temperature (−40 to −10 °C) (reproduced with permission.<sup>19</sup> Copyright 2016, Elsevier).





materials, electronic conductivities can also differ in rutile and anatase.<sup>49</sup>

The absorption coefficient estimated from the reflectance data is used as a quantitative measurement of the optical properties of TiO<sub>2</sub> NPs. Optical band gap of all TiO<sub>2</sub> were obtained using relational expression  $(h\nu F(R_{\infty}))^{(1/n)} = A(h\nu - E_g)$ , where  $A$  is proportional constant depends on the properties of the material,  $h$  is the Planck's constant,  $\nu$  is the frequency of vibration,  $E_g$  is the band gap,  $F(R_{\infty})$  is a Kubelka-Munk function and  $n$  is constant, and it is directly related to the nature of the samples electronic transition.<sup>177</sup> For the allowed direct transition value of  $n$  is 1/2, allowed indirect transition value of  $n$  is 2, forbidden direct transition value of  $n$  is 3/2, and for forbidden indirect transition the value of  $n$  is 3. Since TiO<sub>2</sub> shows the allowed indirect transition, the value of  $n = 2$  was used in this for all TiO<sub>2</sub>. The recorded diffusion spectrum is converted to the Kubelka-Munk function, which is proportional to the absorption coefficient ( $\alpha$ ), and  $R$  is the reflectance of a given wavelength. Using the  $F(R_{\infty})$ , the curve is drawn having a value of  $(h\nu - (h\nu F(R_{\infty}))^{(1/2)})$ , with the help of  $h\nu$  and  $(h\nu F(R_{\infty}))^{(1/2)}$  as the  $X$  and  $Y$  axes, respectively (see Fig. 17a). Here,  $h\nu$  is calculated using  $E = hc/\lambda$ , where  $E$  is the photon energy,  $h$  is Planck's constant,  $c$  is the light intensity and  $\lambda$  is a wavelength.<sup>19</sup>

DFT methods have been explored for electronic structures of TiO<sub>2</sub>, while band gaps of TiO<sub>2</sub> nanoparticles are most popularly measured by UV-vis spectrum. The tetrahedral and octahedral coordinate Ti species gave peaks at 220–260 and 330–400 nm,

respectively, during UV-vis spectrum analysis.<sup>178</sup> A change in the coordination number can be one of the important quality criteria during the formation of crystals. Anatase and rutile consist of octahedral metal centers as building blocks. Preparation conditions and material type govern the optical properties of nano TiO<sub>2</sub>. An indirect-gap semiconductor was made up of natural brookite crystal owing to its excellent optical properties.<sup>179</sup> High-quality brookite, rutile, and anatase showed bandgap energies of  $3.4 \pm 0.1$  eV,  $3.0 \pm 0.1$  eV, and  $3.2 \pm 0.1$  eV, respectively.<sup>180</sup> Visible light was absorbed by prominently oxygen-deficient TiO<sub>2</sub> systems during UV-vis spectroscopy. Spectral characteristics of the visible-light-active TiO<sub>2</sub> photocatalysts initiate from the F-type color centers allied with oxygen positions and Ti-related color centers.<sup>49</sup>

Temperature fluctuation can induce changes in the particle size and defects promote stress in grain boundaries, which ultimately govern the optical bandgap.<sup>181</sup> The optical band gap is also dependent on the difference in interatomic spaces.<sup>19</sup> The specific surface area of nano-titania is measured by BET, as shown in Fig. 17b. The preparation temperature of nano TiO<sub>2</sub> determined the surface area and pore size, and ultimately shape and rate of nucleation. The advantage of the oval-shaped nanoparticles over nanorods is the high surface-to-volume ratio which provides a higher surface area.<sup>19,69</sup>

Among the three polymorphs of titania, the rutile and anatase phase mix are most commonly used due to its synergistic effect having a profound impact on the activity when used as a photocatalyst. Individually, anatase with an approximate bandgap of 3.2 eV shows better photocatalytic activity than the rutile counterpart with approximately 3 eV bandgap. Additionally, these titania polymorphs display a change in the properties with its crystallographic orientation. Morris Hotsenpiller *et al.* discussed thoroughly in their work how rutile TiO<sub>2</sub> films exhibited different properties and photochemical activities depending on the orientations.<sup>182</sup> They observed that rutile with different orientations along the 101, 111 and 001 orientations have higher Ag<sup>+</sup> photoreduction rates in comparison to the 100 and 110 orientations. This is due to the fact that the orientations in the former have better utilization of the photogenerated electron and hole pair required for the photoreduction. Apart from this, it can also be observed that nanomaterials with different orientations have the space charge orientations different, resulting in varying flat band potentials. Therefore, there is more electron and hole separation due to large band bending at the surface. This also results in decreased electron hole recombination. Similarly, anisotropic-dependent photo-reactivity as a result of the change in the electronic structure was studied by Giocondi *et al.*<sup>183</sup> Hengerer *et al.* also studied the flat band potential of anatase TiO<sub>2</sub> with respect to its crystallographic orientation.<sup>184</sup> It have been observed that the charge transfer process occurs on the basis of orientation. TiO<sub>2</sub> anatase with different facets showed different flat band potential in aqueous solution, giving rise to a shift in the onset potential. Additionally, they established that the insertion of ions such as Li<sup>+</sup> on the lattice of anatase TiO<sub>2</sub> is easier in the less dense (001) plane compared to the (101) plane, and there is thus better propagation on the  $c$ -axis. Thus, it can be implied that the

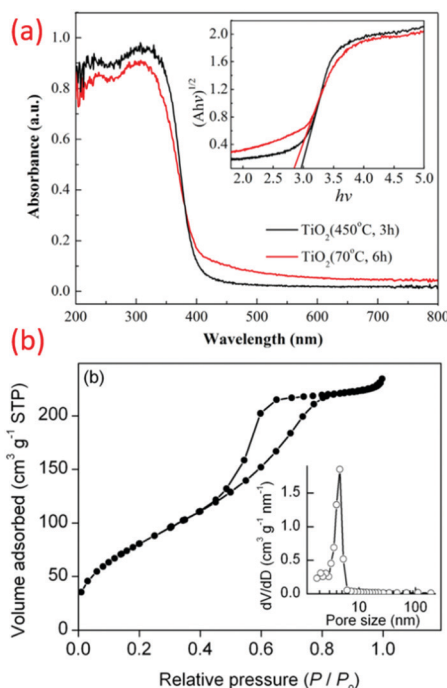


Fig. 17 (a) UV-vis absorbance spectra with inset showing  $h\nu$  and  $(h\nu F(R_{\infty}))^{(1/2)}$  plot of TiO<sub>2</sub> prepared at 70 °C (reproduced with permission.<sup>75</sup> Copyright 2016, Elsevier), (b) N<sub>2</sub> – Adsorption–desorption isotherms with inset showing the pore size distribution of TiO<sub>2</sub> prepared at low (sub-zero) temperature (50 °C) (reproduced with permission.<sup>69</sup> Copyright 2015, Elsevier).



orientation and anisotropy play a very important role in the charge transfer, and consequently has strong relevance to the photocatalysis and charge storage technologies.

## 5. Applications of low temperature TiO<sub>2</sub> nanostructures

### 5.1 Energy harvesting (photovoltaic devices)

Among various photovoltaic devices, low-temperature synthesized titania was found to be applied particularly for dye-sensitized solar cell (DSSC) devices. DSSC is a simple and efficient electrochemical energy conversion device, and its working is inspired from nature by the breakthrough work of O'Regan and Gratzel.<sup>185</sup>

The DSSCs were primarily made of a photoanode, a ruthenium-based molecular dye, an I<sup>−</sup>/I<sup>3−</sup> based liquid electrolyte, and a counter electrode (CE). The photoanode consists of ~12 μm n-type semiconductor oxide with wide bandgap coated on FTO conductive glass substrate. Sunlight is absorbed by dye, which is working as a sensitizer. Electron transfer was facilitated by the electrolyte, while electron transfer was carried out by CE made up of a platinum (Pt) electrocatalyst. Photoexcitation of the dye due to sunlight emits electrons, which flow towards the conduction band of semiconductor. This diffuses through FTO and ultimately reaches CE through an external circuit. The redox electrolyte reduction and subsequent dye-degeneration take place in an external circuit. The crucial part of the DSSC operation is the semiconductor metal oxide. Mainly, the anatase polymorph of TiO<sub>2</sub> is preferred because of the high bandgap energy (3.2 eV) that absorbs only below 388 nm, making it invisible to most of the solar spectrum, thus reducing the recombination rate of photo-injected electrons. Moreover, the anatase phase has a higher conduction band edge energy, which is highly favorable for effective charge separation.

In a particular study by Kovash Jr. *et al.*, a novel synthetic method of developing 4.5 nm sized TiO<sub>2</sub> particles was reported by sol-gel method at 80 °C for DSSC applications.<sup>186</sup> These TiO<sub>2</sub> particles were made into colloids, and thereby deposited as a compact layer for the DSSC photoanode. A power conversion efficiency as high as 5.5% were reported with increased shunt resistance due to decreased electrolyte reduction at the TCO-electrolyte interface and decreased series resistance due to improved electrical contact between the TCO and the TiO<sub>2</sub> photoelectrode. Another interesting study on the low temperature synthesized titania is mainly focused on the anatase-rutile phase proportion of TiO<sub>2</sub>, which is found to be crucial for photovoltaic and photocatalytic applications.<sup>39</sup> Generally, the synthesis of TiO<sub>2</sub> in a highly acidic environment creates a mixture of anatase-brookite and anatase-brookite-rutile crystals with superior photocatalytic activities compared to the commercially available Degussa P25 powder.<sup>126</sup> Furthermore, the rutile nanorod structures showed significant photocatalytic properties compared to the commercial P25. This can be attributed to the high crystallinity with reduced defects. The

small sized nanorods of 10–15 nm were found to be effectively provided with a short electron path. The rutile samples had smaller band gaps, and thus could absorb more light. Additionally, the larger surface area was good enough to provide more active sites for the dye to absorb more light. TiO<sub>2</sub> synthesized by means of glacial acetic acid at relatively low temperature had a large surface area and particles with uniform pore size, as shown in Fig. 18a.<sup>69</sup> The particular structure provides a large number of active sites to adsorb dye molecules. The amount of dye molecules is proportional to the light-harvesting efficiency and such a structure is inevitable to increase the photocurrent, and thus the efficiency of 9.8% for the dye-sensitized solar cells (DSSC).

The first investigation on the synthesis of nano-titania at sub-zero temperature and its application as an anode material for DSSCs were reported by Shejale *et al.*<sup>19</sup> The well-crystallized anatase and rutile TiO<sub>2</sub> nanoparticles fabricated by one-step sub-zero temperature methods were used as photoanodes for DSSC. Remarkable enhancement in the photocurrent density and photoconversion efficiency as high as 8.6%, respectively, was reported. The rutile titanium nanorods prepared using the hydrothermal method of uniform size and highly crystalline nature exhibited remarkable photocatalytic properties over bulk rutile TiO<sub>2</sub>.<sup>74</sup> In the absence of subsequent hydrothermal treatment, anatase TiO<sub>2</sub> NP chains were obtained at low temperatures. High efficiency of this material is due to the large surface area, high dye adsorption, enhanced electron diffusion length, and lower charge recombination. A thin film with greater surface area harvests incident light proficiently, which ultimately increases the efficiency and high photovoltage generation (see Fig. 18b and c).<sup>69</sup>

A DBD jet was used for the deposition of TiO<sub>2</sub> films (30 W RF power) using TiCl<sub>4</sub>/O<sub>2</sub> as the precursors and argon as a plasma generation gas. This method can be simply implemented for the manufacture of TiO<sub>2</sub> films on FTO glass at rates 25 times faster than formerly reported for plasma CVD. About 50% efficiency improvement was observed during photoconversion due to employing this film as photoanodes in DSSC. This efficiency is comparable to commercial TiO<sub>2</sub> nanoparticle photoanodes (P25, Degussa).<sup>113</sup>

Low temperature (100 °C) accessible solution-treated ETL was based on the crystalline np-TiO<sub>2</sub> of the anatase phase for the manufacture of PSCs. Simple, versatile and parameter control (doping) are advantages of the np-TiO<sub>2</sub> synthesis, leading to various hydrodynamic diameters. A control of the synthesis time can produce np-TiO<sub>2</sub> with different sizes. In terms of the PV enactment, high efficiencies (initial PCE: >19%, constant voltage PCE near MPP: 18.2%) are attained by means of spin-coated CH<sub>3</sub>NH<sub>3</sub>PbI<sub>3</sub> as the absorber layer (see Fig. 18d).<sup>100</sup> TiO<sub>2</sub> established a superficial one-step, low-temperature, non-hydrolytic method for *in situ* synthesis. Usually, the CH<sub>3</sub>NH<sub>3</sub>PbI<sub>3</sub> (MAPbI<sub>3</sub>) absorber system consists of TiO<sub>2</sub> ETL. Based on the survey of >30 devices based on pristine TiO<sub>2</sub> ETL, the maximum PCE of 19.61% is achieved (see Fig. 18e).<sup>161</sup>

Another study demonstrated the spin-coatable TiO<sub>2</sub> nanosol for low-temperature solution processable ETL of flexible



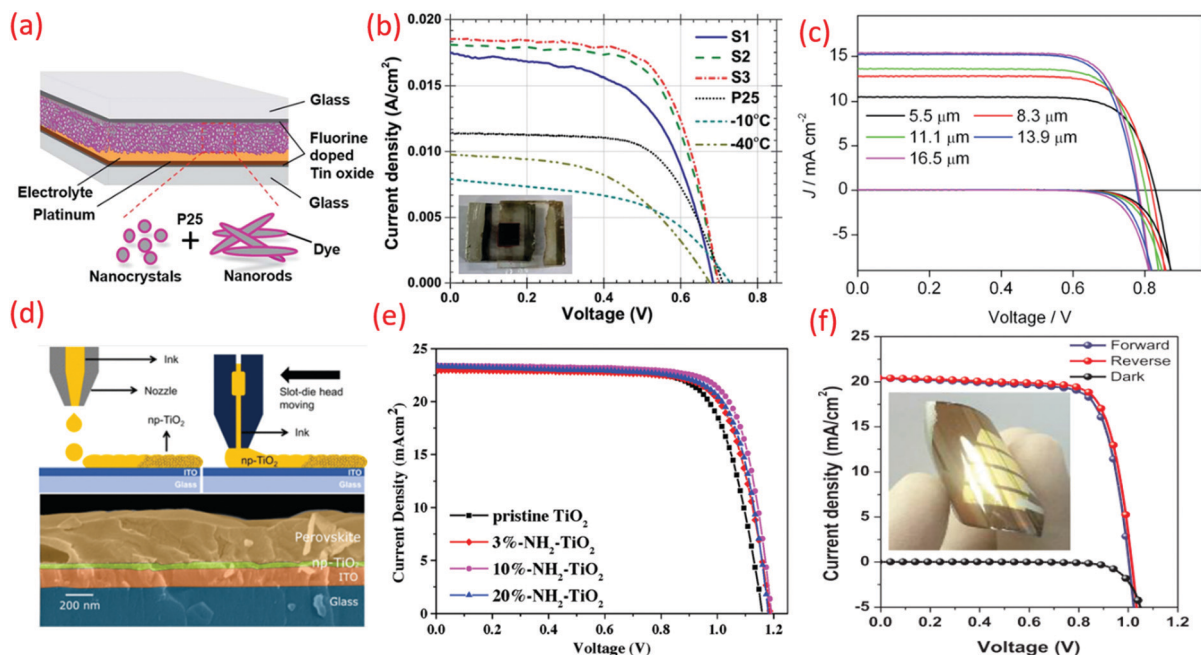


**Fig. 18** (a) Schematic representation of fabricated DSSC, (b) current density–voltage curves of the DSSC consisting of  $-40$  and  $-10$  °C, P25, S1, S2 and S3 samples as photoanodes under one sun illumination (reproduced with permission.<sup>2</sup> Copyright 2016, Royal Society of Chemistry), (c) DSSCs with different film thicknesses from  $\text{TiO}_2$  prepared at  $50$  °C (reproduced with permission.<sup>69</sup> Copyright 2015, Elsevier), (d) the schematic of inkjet printing and slot-die coating of the  $\text{np-TiO}_2$  prepared at low temperature ETL of perovskite solar cells (PSCs) (reproduced with permission.<sup>100</sup> Copyright 2019, American Chemical Society),  $J$ – $V$  curves (e) of the champion devices based on the pristine  $\text{TiO}_2$  and  $\text{NH}_2\text{-TiO}_2$  ETLs. The scanning direction is from open-circuit voltage to short circuit (reverse) (reproduced with permission.<sup>161</sup> Copyright 2019, John Wiley and Sons), (f) of low temperature solution processable  $\text{TiO}_2$  nano-sol for the electron transporting layer of flexible perovskite solar cells (reproduced with permission.<sup>94</sup> Copyright 2019, Elsevier).

perovskite solar cells. The anatase-phased  $\text{TiO}_2$  nanoparticles could be synthesized by peptization in acidic aqueous solution, and the  $\text{TiO}_2$  nano-sols were prepared by re-dispersing the fully dried  $\text{TiO}_2$  nano-powders in  $\text{H}_2\text{O}$ ,  $\text{EtOH}$ ,  $\text{DMSO}$ , and  $\text{DMF}$ . With 10 wt% of  $\text{TiO}_2$  nano-sol in  $\text{DMF}$ , it deposited uniform  $\sim 50$  nm-thick  $\text{TiO}_2$  ETL on ITO/glass by low temperature spin-coating process. The rigid perovskite solar cells composed of glass/ITO/ $\text{TiO}_2$ /perovskite/PTAA/Au exhibited  $22.9 \text{ mA cm}^{-2}$   $J_{\text{sc}}$ ,  $1.04 \text{ V } V_{\text{oc}}$ , 76.6% FF, and 18.2% PCE at 1 Sun condition (see Fig. 18f).<sup>94</sup>

Microwave-assisted sol-gel synthesis produced mesoporous anatase  $\text{TiO}_2$  nano-aggregates without any further hydrothermal treatment and annealing. A high surface area and large size of  $\text{TiO}_2$  were obtained due to extraction by using freeze-drying. The advantage of the high surface area is high dye adsorption in the photoanode. Improvement of the optical path length, reduction of charge recombination, and higher power conversion efficiency (6.16%) are advantages of the larger size of the nanoaggregates.<sup>90</sup>

## 5.2 Photocatalysis

The mechanism of semiconductor photocatalysis comprises four major steps, like light absorption of the semiconductor to generate electron-hole pairs, separation of photoexcited charges, transfer of electrons and holes to the surface of semiconductor, and the effective utilization of charges on the semiconductor surface for redox reactions. To date,  $\text{TiO}_2$  has

been recognized as the most versatile photocatalyst material amongst different oxides owing to its low cost, robust crystal structure and excellent stability, and has accomplished excessive scope for the substantial removal of large organic molecules like dyes, as well as pesticides in a sustainable and cost-effective manner.

The removal of arsenate (V) and fluoride (F<sup>−</sup>) was achieved using  $\text{TiO}_2$  optimized at  $80$  °C hydrolysis temperature and  $0.2 \text{ mol L}^{-1}$   $\text{Ti}(\text{SO}_4)_2$  concentration. Adsorption depended on the pH concentration with the higher adsorption of arsenate (V) and F-occurring at pH 2–8 and pH 3.8, respectively. A faster adsorption was observed at high surface area with uniform  $\text{TiO}_2$  particle sizes.<sup>50</sup> Adsorption of  $>99\%$  of methylene blue was observed by nano  $\text{TiO}_2$  (pH: 2–6) due to the uniform particle size and morphology with a specific surface area and pore size of  $368 \text{ m}^2 \text{ g}^{-1}$  and  $4.2 \text{ nm}$ , respectively. The  $\text{TiO}_2$  NTs crystallinity and photocatalytic characteristics depend on the crystallization temperature and time. Enhanced photocatalytic activities can be achieved at lower crystallization temperature compared to the un-crystallized  $\text{TiO}_2$  NTs (see Fig. 19c).<sup>117</sup>

The fast generation of photoelectroactive titania coatings for the construction of mesoporous  $\text{TiO}_2$  photoanodes is possible in ambient air by means of cold plasma ( $70$  °C). This also forms surface-active sites, which can conduct the chemisorption of water molecules, along with the comprehensive loss of the methyl group. DC magnetron sputtering was carried out at an ambient temperature in the presence of argon gas to prepare





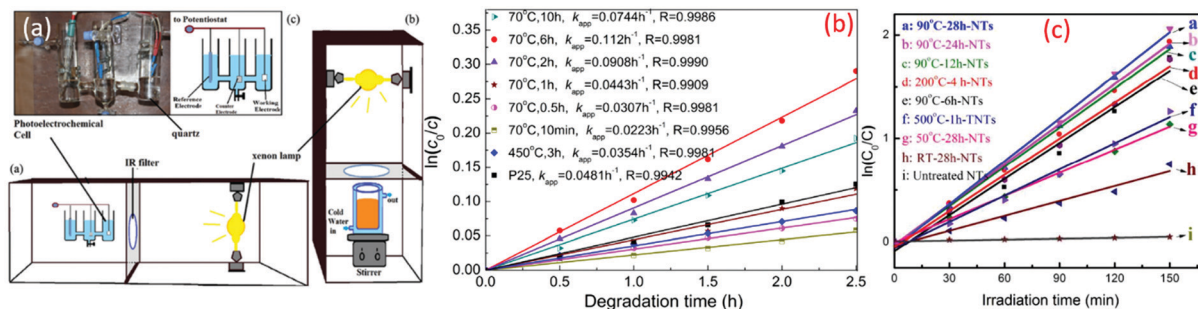


Fig. 19 (a) Schematic representation of the photoelectrochemical setup, a and photocatalytic setup, b and drawing of the photoelectrochemical cell, c (reproduced with permission.<sup>95</sup> Copyright 2016, Taylor & Francis), (b) relationship between  $\ln(C_0/C)$  and photodegradation time of MO in the presence of TiO<sub>2</sub> crystallized at 70 °C for different times (reproduced with permission.<sup>75</sup> Copyright 2016, Elsevier), (c) photocatalytic performance of the TiO<sub>2</sub> NT array films treated with various protocols in the degradation of MO (reproduced with permission.<sup>117</sup> Copyright 2016, American Chemical Society).

the TiO<sub>2</sub> thin film. This film has better performance compared to other TiO<sub>2</sub> films with a rutile layer of 100 nm due to the high separation efficiency of the photogenerated electron and hole pairs and efficient light absorption.<sup>59</sup> A low temperature synthesis without any calcination produces uniform morphology and smaller size NPs due to the influence of acid ions and final peptization. Degrading the RO dye and the anodic photocurrent responses under Xe lamp light irradiation demonstrate the photocatalytic activity and photo-electrochemical properties, respectively (see Fig. 19a).<sup>95</sup> The molar ratios of TiCl<sub>4</sub>, ethanol, and water were adjusted to acquire the rutile TiO<sub>2</sub> nanorod superstructures at low temperatures. The small crystal size, large surface area, narrow band gap, and high crystallinity produced higher photocatalytic activities. The effects of the ions and ethanol on the formation processes of rutile TiO<sub>2</sub> nanorods are proposed.<sup>70</sup>

Mesoporous anatase TiO<sub>2</sub> nanoparticles have been effectively manufactured in water at <90 °C. These nano TiO<sub>2</sub> comprises certain organic residuals. The synthesis temperature and time significantly affect the specific surface areas, while the tetrabutyl titanate concentration did not have a significant effect. This nano TiO<sub>2</sub> has excellent photocatalytic activity compared to commercial TiO<sub>2</sub> (P25) and TiO<sub>2</sub> calcined at 450 °C for 3 h under UV or visible light irradiation, as shown in Fig. 19b.<sup>75</sup>

Low-cost and straightforward sol-gel techniques can prepare anatase TiO<sub>2</sub> NPs by a short crystallization time and low temperature (50 °C). The morphology and structure of these nanoparticles are governed by the precursor concentration and reaction time. Particles prepared at higher precursor concentrations showed the greatest photodegradation of MO because of the small particle size and large surface area. The particle size shows a dynamic role in the photocatalytic activity since the smaller crystals offered greater surface area-to-volume ratios, brought improved surface absorbability of the hydroxyl group, and lowered the electron-hole recombination.<sup>171</sup>

Photochemical synthesis is the use of sunlight to perform chemical reactions, where the electronic excitations occur with light as a chemical reagent. In this process, the ratio of the product formed (in moles) to that of the radiation adsorbed is calculated to be the efficiency of the photochemical reaction.<sup>187</sup> Some of the applications relating to photochemical reactions

include free radical reactions, which allow chemical reactions to occur at lower temperatures and form short radicals. Additionally, photochemical reactions carried out at lower temperature can be beneficial to reduce aggregation in nanoparticles. For example, Li *et al.* reported on the zero-degree photochemical synthesis of Pt/TiO<sub>2</sub>, which are highly dispersed with suppressed aggregation.<sup>188</sup> This was achieved due to a sluggish diffusion-controlled reaction, which was able to control the nucleation and growth. There are various factors that influence the formation, properties and activity of the synthesized nanoparticles. Among the many photochemical reactions, photoreduction using UV irradiation is commonly used.<sup>189</sup> The time and intensity of irradiation determine the intensity of growth and distribution of the photo-deposition. Generally, temperature plays a vital role in the solution-phase reaction in determining the rate of nucleation and growth to regulate the rate of diffusion of the metal ions in the liquid during the photochemical reaction. Increasing the temperature during photo-deposition causes the less stable particles to aggregate, leading to the formation of larger sized nanoparticles. A lower temperature decreases the kinetics of nuclei formation and restricts the growth rate, preventing nanoparticle aggregation. Controlling the temperature can regulate the thermodynamics and kinetics, providing stability and high activity for superior performance in catalytic reactions. Ko *et al.* synthesized Ag/TiO<sub>2</sub> using UV irradiation for photochemical reduction and deposition at room temperature.<sup>190</sup> Various environmental photochemical applications of TiO<sub>2</sub>, such as dye degradation and water treatment, are used. However, the applications of TiO<sub>2</sub> are not limited to these and extend to various spheres, including solar cells as photocatalysts in dye-sensitized solar cells, quantum dot solar cells, and perovskite solar cells. Additionally, modified TiO<sub>2</sub> is used for applications, such as composites of metal and TiO<sub>2</sub> for CO oxidation and antibacterial application.<sup>191</sup>

### 5.3 Energy storage

Owing to the high energy density and long cycle life, lithium-ion batteries have substituted many battery technologies used in our day-to-day technology-based devices, like laptops and cell phones. However, conventional lithium-ion batteries lack high power and superior energy density for applications as storage devices for solar and wind energy, as well as for electric



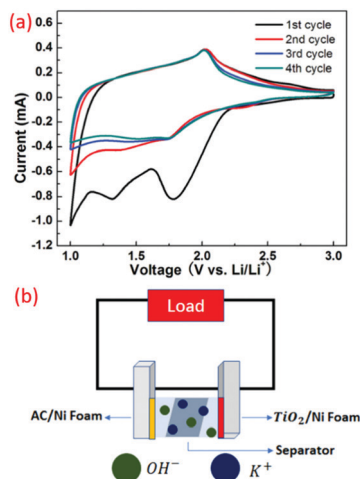


**Fig. 20** (a) The electrochemical properties of the as-prepared HM-TiO<sub>2</sub>-NB (reproduced with permission.<sup>107</sup> Copyright 2015, Elsevier). (b) Assembly of the asymmetric supercapacitor, where AC as cathode and TiO<sub>2</sub> nanocrystals were prepared at low temperature (reproduced with permission.<sup>96</sup> Copyright 2019, Elsevier).

vehicles. In this regard, advanced nanostructured materials with fast charge–discharge capability and high capacity have been of particular interest. Notably, various polymorphs of TiO<sub>2</sub> have been widely considered as anode materials for lithium-ion batteries due to their advantages, like low cost, safety, and high-rate capability. By lowering the processing temperature of titania, we can still make the battery fabrication more cost-effective. It has been proved that the structure of TiO<sub>2</sub> that has a hybrid of amorphous and crystalline phases of TiO<sub>2</sub> fabricated at very low temperatures displayed amazing electrochemical properties, and found application as an anode material for Li-ion batteries (see Fig. 20).<sup>96,105</sup> The nanobundle structures of titania were found to be quite stable and exhibited high reversible properties even after many charge–discharge cycles, and are a promising material for Li-ion battery applications. The high storage capacity was because of the large specific surface area and the amorphous layer over the nanowires, which provide many active sites for Li<sup>+</sup> insertion. The porous straight channel structure helps in the penetration of electrolytes and the adsorption of Li ions.

## 6. Conclusions and perspectives

Titania (TiO<sub>2</sub>) continues to be one of the most contemplated nanomaterials in recent decades. However, in order to obtain high-performing nanomaterials, it is important to optimize and control the synthetic protocols to prepare the desired titania having controlled morphology, phase, size, and other properties. Temperature-based synthesis approaches include the sol–gel at sub-zero temperature to room temperature with high applications. Therefore, it can be very well established that by precisely controlling the synthesis methods, TiO<sub>2</sub> can be modified to have enhanced performance for the designated application. This review has featured the essential approaches

for the synthesis of titania at low temperatures, and used it for various applications. Interesting effects, such as phase and morphology variation as a factor of temperature difference, have been presented here and give specific insights into the low-temperature TiO<sub>2</sub> crystallinity. However, there lies a great challenge in the study and correlation of the synthetic procedure and with performance analysis when used for applications such as in solar cells. Overcoming these challenges by means of low-temperature synthesis of TiO<sub>2</sub> will significantly improve the cost-effectiveness without compromising the effectiveness when used as electrode materials in various applications.

## Author contributions

K. P. S. conceived the review framework, curated the data, and structured the figures accordingly. R. K., H. P., D. L., and P. R. carried out writing the original draft and formal analysis and investigation. R. K. S. supervised and acquired the funding. All authors discussed and commented on the work during the drafting of the manuscript.

## Conflicts of interest

The authors declare no competing conflicts of interest.

## Acknowledgements

The authors would like to acknowledge support from the Department of Chemistry, Indian Institute of Technology Jodhpur for this study. The authors are grateful for financial support from SERB-CRG-India (grant number CRG/2020/002163) and DBT PAN IIT Center for Bioenergy (grant number BT/PR41982/PBD/26/822/2021).

## Notes and references

- 1 S. M. Gupta and M. Tripathi, *Chin. Sci. Bull.*, 2011, **56**, 1639.
- 2 K. P. Shejale, D. Laishram and R. K. Sharma, *RSC Adv.*, 2016, **6**, 23459–23466.
- 3 A. J. Haider, Z. N. Jameel and I. H. M. Al-Hussaini, *Energy Procedia*, 2019, **157**, 17–29.
- 4 J. Cai, J. Shen, X. Zhang, Y. H. Ng, J. Huang, W. Guo, C. Lin and Y. Lai, *Small Methods*, 2019, **3**, 1800184.
- 5 A. Fujishima and K. Honda, *Nature*, 1972, **238**, 37–38.
- 6 T. Matsunaga, R. Tomoda, T. Nakajima and H. Wake, *FEMS Microbiol. Lett.*, 1985, **29**, 211–214.
- 7 A. Fujishima, *Photomed. Photobiol.*, 1986, **8**, 45–46.
- 8 Y. Ma, X. Wang, Y. Jia, X. Chen, H. Han and C. Li, *Chem. Rev.*, 2014, **114**, 9987–10043.
- 9 H. Zhang and J. F. Banfield, *Chem. Rev.*, 2014, **114**, 9613–9644.
- 10 A. Vittadini, M. Casarin and A. Selloni, *J. Phys. Chem. C*, 2009, **113**, 18973–18977.



- 11 M. Mezhericher, J. K. Nunes, J. J. Guzowski and H. A. Stone, *Chem. Eng. J.*, 2018, **346**, 606–620.
- 12 Y. Zhang, *Integr. Ferroelectr.*, 2015, **160**, 142–146.
- 13 K. P. Shejale, D. Laishram, R. Gupta and R. K. Sharma, *ChemistrySelect*, 2018, **3**, 7291–7301.
- 14 D. Laishram, K. P. Shejale, R. K. Sharma and R. Gupta, *RSC Adv.*, 2016, **6**, 78768–78773.
- 15 R. Krishnapriya, S. Praneetha and A. Vadivel Murugan, *Inorg. Chem. Front.*, 2017, **4**, 1665–1678.
- 16 D. Laishram, K. P. Shejale, R. Gupta and R. K. Sharma, *Mater. Lett.*, 2018, **231**, 225–228.
- 17 L. F. Trierweiler and J. O. Trierweiler, in *Nanocosmetics and Nanomedicines: New Approaches for Skin Care*, ed. R. Beck, S. Guterres and A. Pohlmann, Springer Berlin Heidelberg, Berlin, Heidelberg, 2011, DOI: 10.1007/978-3-642-19792-5\_6, pp. 123–138.
- 18 M. Mezhericher, *Eur. J. Pharm. Biopharm.*, 2014, **88**, 866–878.
- 19 K. P. Shejale, D. Laishram, M. S. Roy, M. Kumar and R. K. Sharma, *Mater. Des.*, 2016, **92**, 535–540.
- 20 X. Chen, *Chin. J. Catal.*, 2009, **30**, 839–851.
- 21 X. Wang, Z. Li, J. Shi and Y. Yu, *Chem. Rev.*, 2014, **114**, 9346–9384.
- 22 L. Liu and X. Chen, *Chem. Rev.*, 2014, **114**, 9890–9918.
- 23 X. Chen and S. S. Mao, *Chem. Rev.*, 2007, **107**, 2891–2959.
- 24 M. Cargnello, T. R. Gordon and C. B. Murray, *Chem. Rev.*, 2014, **114**, 9319–9345.
- 25 I. Ali, M. Suhail, Z. A. Allothman and A. Alwarthan, *RSC Adv.*, 2018, **8**, 30125–30147.
- 26 A. K. Wahab, S. Ould-Chikh, K. Meyer and H. Idriss, *J. Catal.*, 2017, **352**, 657–671.
- 27 D. Reyes-Coronado, G. Rodríguez-Gattorno, M. E. Espinosa-Pesqueira, C. Cab, R. de Coss and G. Oskam, *Nanotechnology*, 2008, **19**, 145605.
- 28 M. Pal, J. García Serrano, P. Santiago and U. Pal, *J. Phys. Chem. C*, 2007, **111**, 96–102.
- 29 M. Mattesini, J. S. de Almeida, L. Dubrovinsky, N. Dubrovinskaia, B. Johansson and R. Ahuja, *Phys. Rev. B: Condens. Matter Mater. Phys.*, 2004, **70**, 212101.
- 30 J. K. Dewhurst and J. E. Lowther, *Phys. Rev. B: Condens. Matter Mater. Phys.*, 1996, **54**, R3673–r3675.
- 31 S. K. Filatov, N. A. Bendeliani, B. Albert, J. Kopf, T. I. Dyuzheva and L. M. Lityagina, *Dokl. Phys.*, 2007, **52**, 195–199.
- 32 V. Swamy, L. S. Dubrovinsky, N. A. Dubrovinskaia, F. Langenhorst, A. S. Simionovici, M. Drakopoulos, V. Dmitriev and H.-P. Weber, *Solid State Commun.*, 2005, **134**, 541–546.
- 33 M. Latroche, L. Brohan, R. Marchand and M. Tournoux, *J. Solid State Chem.*, 1989, **81**, 78–82.
- 34 J. Akimoto, Y. Gotoh, Y. Oosawa, N. Nonose, T. Kumagai, K. Aoki and H. Takei, *J. Solid State Chem.*, 1994, **113**, 27–36.
- 35 X. Wang, Z. Li, J. Shi and Y. Yu, *Chem. Rev.*, 2014, **114**, 9346–9384.
- 36 S. León-Ríos, R. Espinoza González, S. Fuentes, E. Chávez Ángel, A. Echeverría, A. E. Serrano, C. S. Demergasso and R. A. Zárate, *J. Nanomater.*, 2016, **2016**, 7213672.
- 37 C.-T. Dinh, T.-D. Nguyen, F. Kleitz and T.-O. Do, *ACS Nano*, 2009, **3**, 3737–3743.
- 38 G. Li, L. Li, J. Boerio-Goates and B. F. Woodfield, *J. Am. Chem. Soc.*, 2005, **127**, 8659–8666.
- 39 D. A. H. Hanaor and C. C. Sorrell, *J. Mater. Sci.*, 2011, **46**, 855–874.
- 40 X. Kang, S. Liu, Z. Dai, Y. He, X. Song and Z. Tan, *Catalysts*, 2019, **9**(2), 191.
- 41 V. Jouenne, J.-L. Duvail, L. Brohan, E. Gautron and M. Richard-Plouet, *RSC Adv.*, 2015, **5**, 15118–15125.
- 42 J. Buckeridge, K. T. Butler, C. R. A. Catlow, A. J. Logsdail, D. O. Scanlon, S. A. Shevlin, S. M. Woodley, A. A. Sokol and A. Walsh, *Chem. Mater.*, 2015, **27**, 3844–3851.
- 43 J. Pan, G. Liu, G. Q. Lu and H. M. Cheng, *Angew. Chem., Int. Ed. Engl.*, 2011, **50**, 2133–2137.
- 44 M. Pawar, S. Topcu Sandoğdular and P. Gouma, *J. Nanomater.*, 2018, **2018**, 5953609.
- 45 V. Etacheri, C. Di Valentin, J. Schneider, D. Bahnemann and S. C. Pillai, *J. Photochem. Photobiol., C*, 2015, **25**, 1–29.
- 46 S. A. Ansari and M. H. Cho, *Sci. Rep.*, 2016, **6**, 25405.
- 47 C. Cavallo, F. Di Pascasio, A. Latini, M. Bonomo and D. Dini, *J. Nanomater.*, 2017, **2017**, 5323164.
- 48 Y. Bai, I. Mora-Seró, F. De Angelis, J. Bisquert and P. Wang, *Chem. Rev.*, 2014, **114**, 10095–10130.
- 49 L. Sang, Y. Zhao and C. Burda, *Chem. Rev.*, 2014, **114**, 9283–9318.
- 50 H. Deng, K. Zhang and X. Wang, *Desalin Water Treat*, 2016, **57**, 9409–9419.
- 51 E. Binetti, N. Bazzanella, R. Comparelli and A. Miotello, *Mater. Lett.*, 2016, **174**, 226–229.
- 52 P. Dong, X. Cheng, Z. Huang, Y. Chen, Y. Zhang, X. Nie and X. Zhang, *Mater. Res. Bull.*, 2018, **97**, 89–95.
- 53 S. Liu, J. Yu and M. Jaroniec, *Chem. Mater.*, 2011, **23**, 4085–4093.
- 54 G. Moon, Y.-C. Cho, J.-Y. Lee and J. Kang, *Mater. Trans.*, 2019, **60**, 988–996.
- 55 D. Vorkapic and T. Matsoukas, *J. Am. Chem. Soc.*, 1998, **81**, 2815–2820.
- 56 E. Burunkaya, M. Akarsu, H. Erdem Çamurlu, Ö. Kesmez, Z. Yeşil, M. Asiltürk and E. Arpaç, *Appl. Surf. Sci.*, 2013, **265**, 317–323.
- 57 C. Cantau, T. Pigot, J.-C. Dupin and S. Lacombe, *J. Photochem. Photobiol., A*, 2010, **216**, 201–208.
- 58 B. K. Mutuma, G. N. Shao, W. D. Kim and H. T. Kim, *J. Colloid Interface Sci.*, 2015, **442**, 1–7.
- 59 W. Hui, S. Guodong, Z. Xiaoshu, Z. Wei, H. Lin and Y. Ying, *J. Environ. Sci.*, 2017, **60**, 33–42.
- 60 P. Pookmanee, I. Phiwchai, S. Yoriya, R. Puntharod, S. Sangsrichan and S. Phanichphant, *Ferroelectrics*, 2013, **457**, 30–38.
- 61 U. Diebold, *Surf. Sci. Rep.*, 2003, **48**, 53–229.
- 62 D. O. Scanlon, C. W. Dunnill, J. Buckeridge, S. A. Shevlin, A. J. Logsdail, S. M. Woodley, C. R. A. Catlow, M. J. Powell, R. G. Palgrave, I. P. Parkin, G. W. Watson, T. W. Keal, P. Sherwood, A. Walsh and A. A. Sokol, *Nat. Mater.*, 2013, **12**, 798–801.





- 63 Y.-w. Jun, M. F. Casula, J.-H. Sim, S. Y. Kim, J. Cheon and A. P. Alivisatos, *J. Am. Chem. Soc.*, 2003, **125**, 15981–15985.
- 64 A. Chemseddine and T. Moritz, *Eur. J. Inorg. Chem.*, 1999, 235–245.
- 65 J. Li, Z. Wang, J. Wang and T.-K. Sham, *J. Phys. Chem. C*, 2016, **120**, 22079–22087.
- 66 S. Yin, R. Li, Q. He and T. Sato, *Mater. Chem. Phys.*, 2002, **75**, 76–80.
- 67 S. Y. Choi, M. Mamak, N. Coombs, N. Chopra and G. A. Ozin, *Adv. Funct. Mater.*, 2004, **14**, 335–344.
- 68 M. Pal, J. García Serrano, P. Santiago and U. Pal, *J. Phys. Chem. C*, 2007, **111**, 96–102.
- 69 Y. Cui, L. Zhang, K. Lv, G. Zhou and Z.-S. Wang, *J. Mater. Chem. A*, 2015, **3**, 4477–4483.
- 70 Y. Wang, L. Zhang, K. Deng, X. Chen and Z. Zou, *J. Phys. Chem. C*, 2007, **111**, 2709–2714.
- 71 Y. Brahmi, N. Katir, M. Ianchuk, V. Collière, E. M. Essassi, A. Ouali, A.-M. Caminade, M. Bousmina, J. P. Majoral and A. El Kadib, *Nanoscale*, 2013, **5**, 2850–2856.
- 72 S. Yin, H. Hasegawa, D. Maeda, M. Ishitsuka and T. Sato, *J. Photochem. Photobiol., A*, 2004, **163**, 1–8.
- 73 H. Imai, Y. Takei, K. Shimizu, M. Matsuda and H. Hirashima, *J. Mater. Chem.*, 1999, **9**, 2971–2972.
- 74 L. Bu, W. Yang and H. Ming, *RSC Adv.*, 2015, **5**, 45122–45128.
- 75 Q. Luo, Y. Chen, D. Wang, J. An, X. Li, R. Yin and L. Shi, *Mater. Res. Bull.*, 2015, **67**, 140–145.
- 76 M.-Q. Wang, J. Yan, H.-P. Cui and S.-G. Du, *Mater. Charact.*, 2013, **76**, 39–47.
- 77 P. D. Cozzoli, A. Kornowski and H. Weller, *J. Am. Chem. Soc.*, 2003, **125**, 14539–14548.
- 78 C. Wessel, L. Zhao, S. Urban, R. Ostermann, I. Djerdj, B. M. Smarsly, L. Chen, Y.-S. Hu and S. Sallard, *Chem. – Eur. J.*, 2011, **17**, 775–779.
- 79 C. Leyva-Porras, A. Toxqui-Teran, O. Vega-Becerra, M. Miki-Yoshida, M. Rojas-Villalobos, M. García-Guaderrama and J. A. Aguilar-Martínez, *J. Alloys Compd.*, 2015, **647**, 627–636.
- 80 H. K. Park, Y. T. Moon, D. K. Kim and C. H. Kim, *J. Am. Ceram. Soc.*, 1996, **79**, 2727–2732.
- 81 T. Homola, P. Dzik, M. Veselý, J. Kelar, M. Černák and M. Weiter, *ACS Appl. Mater. Interfaces*, 2016, **8**, 33562–33571.
- 82 S. Patra, C. Andriamiadamanana, M. Tulodziecki, C. Davoisne, P.-L. Taberna and F. Sauvage, *Sci. Rep.*, 2016, **6**, 21588.
- 83 X. Zhang, Y. Chen, H. Lei, S. Zhao, F. Han, X. Xiang, Y. Zhao, N. Huang and G. Wan, *Mater. Des.*, 2016, **89**, 476–484.
- 84 S. Yin, H. Hasegawa and T. Sato, *Chem. Lett.*, 2002, 564–565.
- 85 Y. Li, Z. Qin, H. Guo, H. Yang, G. Zhang, S. Ji and T. Zeng, *PLoS One*, 2014, **9**, e114638.
- 86 T. Hirai, H. Sato and I. Komasaawa, *Ind. Eng. Chem. Res.*, 1993, **32**, 3014–3019.
- 87 A. E. Danks, S. R. Hall and Z. Schnepf, *Mater. Horiz.*, 2016, **3**, 91–112.
- 88 S. Doeuff, M. Henry, C. Sanchez and J. Livage, *J. Non-Cryst. Solids*, 1987, **89**, 206–216.
- 89 W. Huang, X. Tang, Y. Wang, Y. Kolytyn and A. Gedanken, *Chem. Commun.*, 2000, 1415–1416, DOI: 10.1039/B003349I.
- 90 D. N. Joshi and R. Arun Prasath, *Mater. Today: Proc.*, 2016, **3**, 2413–2421.
- 91 S.-Q. Hu, G.-F. Li, X.-H. Chang and L.-F. Ma, *Inorg. Nano-Met. Chem.*, 2017, **47**, 328–331.
- 92 V. Purcar, V. Rădițoiu, A. Dumitru, C.-A. Nicolae, A. N. Frone, M. Anastasescu, A. Rădițoiu, M. F. Raduly, R. A. Gabor and S. Căprărescu, *Appl. Surf. Sci.*, 2019, **487**, 819–824.
- 93 Q.-E. Zhao, W. Wen, Y. Xia and J.-M. Wu, *Thin Solid Films*, 2018, **648**, 103–107.
- 94 M. S. You, J. H. Heo, J. K. Park, S. H. Moon, B. J. Park and S. H. Im, *Sol. Energy Mater. Sol. Cells*, 2019, **194**, 1–6.
- 95 H. Bazrafshan, Z. Alipour Tesieh, S. Dabirnia and A. Naderifar, *Mater. Manuf. Process.*, 2016, **31**, 119–125.
- 96 I. Heng, C. W. Lai, J. C. Juan, A. Numan, J. Iqbal and E. Y. L. Teo, *Ceram. Int.*, 2019, **45**, 4990–5000.
- 97 Z. Wang, B. Huang, Y. Dai, X. Zhang, X. Qin, Z. Li, Z. Zheng, H. Cheng and L. Guo, *CrystEngComm*, 2012, **14**, 4578–4581.
- 98 D. Depan, *Bioinspired, Biomimetic Nanobiomater.*, 2015, **4**, 121–132.
- 99 C. She, J. Guo and T. Lian, *J. Phys. Chem. C*, 2007, **111**, 6903–6912.
- 100 I. M. Hossain, D. Hudry, F. Mathies, T. Abzieher, S. Moghadamzadeh, D. Rueda-Delgado, F. Schackmar, M. Bruns, R. Andriessen, T. Aernouts, F. Di Giacomo, U. Lemmer, B. S. Richards, U. W. Paetzold and A. Hadipour, *ACS Appl. Energy Mater.*, 2019, **2**, 47–58.
- 101 A. Mehrzad, A. A. Khakpoor, S. Mortazavi and M. Rasooli, *J. Nanoelectron. Optoelectron.*, 2018, **13**, 156–162.
- 102 T. Gupta, Samriti, J. Cho and J. Prakash, *Mater. Today Chem.*, 2021, **20**, 100428.
- 103 Z.-Y. Ma, Z.-L. Yu, Z.-L. Xu, L.-F. Bu, H.-R. Liu, Y.-B. Zhu, B. Qin, T. Ma, H.-J. Zhan, L. Xu, H.-A. Wu, H. Ding and S.-H. Yu, *Matter*, 2020, **2**, 1270–1282.
- 104 X. Shen, J. Zhang and B. Tian, *J. Hazard. Mater.*, 2011, **192**, 651–657.
- 105 J. Jin, S.-Z. Huang, J. Liu, Y. Li, L.-H. Chen, Y. Yu, H.-E. Wang, C. P. Grey and B.-L. Su, *Adv. Sci.*, 2015, **2**, 1500070.
- 106 D. Fattakhova-Rohlfing, A. Zaleska and T. Bein, *Chem. Rev.*, 2014, **114**, 9487–9558.
- 107 M. Hu, J. Xu, J. Gao, S. Yang, J. S. P. Wong and R. K. Y. Li, *Dalton Trans.*, 2013, **42**, 9777–9784.
- 108 K. Safeen, V. Micheli, R. Bartali, G. Gottardi and N. Laidani, *J. Phys. D: Appl. Phys.*, 2015, **48**, 295201.
- 109 T. S. Bonelli and I. Pereyra, *Appl. Surf. Sci.*, 2018, **442**, 239–244.
- 110 K. M. Krause, M. T. Taschuk and M. J. Brett, *J. Vac. Sci. Technol., A*, 2013, **31**, 031507.
- 111 A. Ishii, I. Oikawa, M. Imura, T. Kanai and H. Takamura, *Mater. Trans.*, 2018, **59**, 33–38.
- 112 K. Robbie and M. J. Brett, *J. Vac. Sci. Technol., A*, 1997, **15**, 1460–1465.



- 113 H.-K. Seo, C. M. Elliott and H.-S. Shin, *ACS Appl. Mater. Interfaces*, 2010, **2**, 3397–3400.
- 114 L.-B. Di, X.-S. Li, C. Shi, Y. Xu, D.-Z. Zhao and A.-M. Zhu, *J. Phys. D: Appl. Phys.*, 2008, **42**, 032001.
- 115 L. Besra and M. Liu, *Prog. Mater. Sci.*, 2007, **52**, 1–61.
- 116 S. Cabanas-Polo and A. R. Boccaccini, *J. Eur. Ceram. Soc.*, 2016, **36**, 265–283.
- 117 Y. Liao, X. Wang, Y. Ma, J. Li, T. Wen, L. Jia, Z. Zhong, L. Wang and D. Zhang, *Cryst. Growth Des.*, 2016, **16**, 1786–1791.
- 118 M. Inoue, in *Handbook of Advanced Ceramics*, Second Edition, ed. S. Somiya, Academic Press, Oxford, 2013, DOI: 10.1016/B978-0-12-385469-8.00050-2, pp. 927–948.
- 119 C. T. Nam, W.-D. Yang and L. M. Duc, *J. Nanomater.*, 2013, **2013**, 627385.
- 120 N. Katir, N. Marcotte, S. Michlewska, M. Ionov, N. El Brahmi, M. Bousmina, J. P. Majoral, M. Bryszewska and A. El Kadib, *ACS Appl. Nano Mater.*, 2019, **2**, 2979–2990.
- 121 D. Velasco-Arias, I. Zumeta-Dubé, D. Díaz, P. Santiago-Jacinto, V.-F. Ruiz-Ruiz, S.-E. Castillo-Blum and L. Rendón, *J. Phys. Chem. C*, 2012, **116**, 14717–14727.
- 122 A. Anouar, N. Katir, A.-S. Mamede, A. Aboulaich, K. Draoui, S. Royer and A. El Kadib, *Mater. Chem. Front.*, 2019, **3**, 242–250.
- 123 S. Lettieri, V. Gargiulo, M. Alfè, M. Amati, P. Zeller, V.-A. Maraloiu, F. Borbone, M. Pavone, A. B. Muñoz-García and P. Maddalena, *J. Phys. Chem. C*, 2020, **124**, 3564–3576.
- 124 L. Ge, M. Xu, M. Sun and H. Fang, *J. Solgel Sci. Technol.*, 2006, **38**, 47–53.
- 125 J. Xu, Y. Ao, D. Fu and C. Yuan, *J. Phys. Chem. Solids*, 2008, **69**, 2366–2370.
- 126 K. Fischer, A. Gawel, D. Rosen, M. Krause, A. Abdul Latif, J. Griebel, A. Prager and A. Schulze, *Catalysts*, 2017, **7**(7), 209.
- 127 B. Qi, L. Wu, Y. Zhang, Q. Zeng and J. Zhi, *J. Colloid Interface Sci.*, 2010, **345**, 181–186.
- 128 S. Park, J. Park, J. Heo, B. Y. Hong and J. Hong, *Appl. Surf. Sci.*, 2017, **425**, 547–552.
- 129 Z. Lei, B. Chen, Y. Koo and D. R. MacFarlane, *Chem. Rev.*, 2017, **117**, 6633–6635.
- 130 X. Duan, J. Ma, J. Lian and W. Zheng, *CrystEngComm*, 2014, **16**, 2550–2559.
- 131 M. Paszkiewicz, J. Łuczak, W. Lisowski, P. Patyk and A. Zaleska-Medynska, *Appl. Catal., B*, 2016, **184**, 223–237.
- 132 Y. Zhou and M. Antonietti, *J. Am. Chem. Soc.*, 2003, **125**, 14960–14961.
- 133 T. Nakashima and N. Kimizuka, *J. Am. Chem. Soc.*, 2003, **125**, 6386–6387.
- 134 M. Paszkiewicz-Gawron, M. Długokęcka, W. Lisowski, M. C. Paganini, E. Giamello, T. Klimczuk, M. Paszkiewicz, E. Grabowska, A. Zaleska-Medynska and J. Łuczak, *ACS Sustainable Chem. Eng.*, 2018, **6**, 3927–3937.
- 135 R. Ramanathan and V. Bansal, *RSC Adv.*, 2015, **5**, 1424–1429.
- 136 J. Yu, Q. Li, S. Liu and M. Jaroniec, *Chem. – Eur. J.*, 2013, **19**, 2433–2441.
- 137 N. Kaur and V. Singh, *New J. Chem.*, 2017, **41**, 2844–2868.
- 138 I. Bilecka and M. Niederberger, *Nanoscale*, 2010, **2**, 1358–1374.
- 139 S. Komarneni, R. Roy and Q. H. Li, *Mater. Res. Bull.*, 1992, **27**, 1393–1405.
- 140 C.-C. Chung, T.-W. Chung and T. C. K. Yang, *Ind. Eng. Chem. Res.*, 2008, **47**, 2301–2307.
- 141 Y. Liu, S. Yang, J. Hong and C. Sun, *J. Hazard. Mater.*, 2007, **142**, 208–215.
- 142 A. Jena, R. Vinu, S. A. Shivashankar and G. Madras, *Ind. Eng. Chem. Res.*, 2010, **49**, 9636–9643.
- 143 P. M. P. Danty, A. Mazel, B. Cormary, M. L. De Marco, J. Allouche, D. Flahaut, J. Jimenez-Lamana, S. Lacomme, M.-H. Delville and G. L. Drisko, *Inorg. Chem.*, 2020, **59**, 6232–6241.
- 144 M. I. Dar, A. K. Chandiran, M. Grätzel, M. K. Nazeeruddin and S. A. Shivashankar, *J. Mater. Chem. A*, 2014, **2**, 1662–1667.
- 145 C.-H. Huang, Y.-T. Yang and R.-A. Doong, *Microporous Mesoporous Mater.*, 2011, **142**, 473–480.
- 146 X. Wang, J. Tian, C. Fei, L. Lv, Y. Wang and G. Cao, *RSC Adv.*, 2015, **5**, 8622–8629.
- 147 S. Yoon, E.-S. Lee and A. Manthiram, *Inorg. Chem.*, 2012, **51**, 3505–3512.
- 148 J. H. Bang and K. S. Suslick, *Adv. Mater.*, 2010, **22**, 1039–1059.
- 149 H. Xu, B. W. Zeiger and K. S. Suslick, *Chem. Soc. Rev.*, 2013, **42**, 2555–2567.
- 150 K. S. Suslick and G. J. Price, *Annu. Rev. Mater. Sci.*, 1999, **29**, 295–326.
- 151 W. Huang, X. Tang, Y. Wang, Y. Kolytyn and A. Gedanken, *Chem. Commun.*, 2000, 1415–1416, DOI: 10.1039/B003349I.
- 152 W. H. Suh and K. S. Suslick, *J. Am. Chem. Soc.*, 2005, **127**, 12007–12010.
- 153 J. C. Yu, L. Zhang and J. Yu, *Chem. Mater.*, 2002, **14**, 4647–4653.
- 154 M. Niederberger and G. Garnweitner, *Chem. – Eur. J.*, 2006, **12**, 7282–7302.
- 155 D. Koziej, F. Fischer, N. Kränzlin, W. R. Caseri and M. Niederberger, *ACS Appl. Mater. Interfaces*, 2009, **1**, 1097–1104.
- 156 I. Djerdj, D. Arçon, Z. Jagličić and M. Niederberger, *J. Solid State Chem.*, 2008, **181**, 1571–1581.
- 157 M. Niederberger, M. H. Bartl and G. D. Stucky, *Chem. Mater.*, 2002, **14**, 4364–4370.
- 158 S. Sandhu, N. Kumar, V. P. Singh and V. Singh, *Vacuum*, 2021, **184**, 109896.
- 159 D. C. Hague and M. J. Mayo, *J. Am. Ceram. Soc.*, 1994, **77**, 1957–1960.
- 160 J. Jiang, M. Long, D. Wu and W. Cai, *J. Mol. Catal. A: Chem.*, 2011, **335**, 97–104.
- 161 W. Hu, W. Zhou, X. Lei, P. Zhou, M. Zhang, T. Chen, H. Zeng, J. Zhu, S. Dai, S. Yang and S. Yang, *Adv. Mater.*, 2019, **31**, 1806095.
- 162 A. Soloviev, D. Ivanov, R. Tufeu and A. V. Kanaev, *J. Mater. Sci. Lett.*, 2001, **20**, 905–906.
- 163 S. G. Kumar and K. S. R. K. Rao, *Nanoscale*, 2014, **6**, 11574–11632.
- 164 J. Y. Rempel, M. G. Bawendi and K. F. Jensen, *J. Am. Chem. Soc.*, 2009, **131**, 4479–4489.



- 165 A. Forgács, K. Moldován, P. Herman, E. Baranyai, I. Fábrián, G. Lente and J. Kalmár, *J. Phys. Chem. C*, 2018, **122**, 19161–19170.
- 166 M. Visca and E. Matijević, *J. Colloid Interface Sci.*, 1979, **68**, 308–319.
- 167 E. A. Barringer and H. K. Bowen, *J. Am. Ceram. Soc.*, 1982, **65**, C-199–C-201.
- 168 J. H. Jean and T. A. Ring, *Langmuir*, 1986, **2**, 251–255.
- 169 S. Mahshid, M. Askari and M. S. Ghamsari, *J. Mater. Process. Technol.*, 2007, **189**, 296–300.
- 170 S. Lee, C. Jeon and Y. Park, *Chem. Mater.*, 2004, **16**, 4292–4295.
- 171 Z. Wang, D. Xia, G. Chen, T. Yang and Y. Chen, *Mater. Chem. Phys.*, 2008, **111**, 313–316.
- 172 Y. Prabhu, K. Rao, V. Kumar and B. Kumari, *World J. Nano Sci. Eng.*, 2014, **4**, 21–28.
- 173 Y. T. Prabhu, K. V. Rao, V. S. S. Kumar and B. S. Kumari, *Int. J. Eng. Adv. Technol.*, 2013, **2**, 268–274.
- 174 V. D. Mote, Y. Purushotham and B. N. Dole, *J. Theor. Appl. Phys.*, 2012, **6**, 6.
- 175 W. Qin and J. A. Szpunar, *Philos. Mag. Lett.*, 2005, **85**, 649–656.
- 176 N. A. Deskins, R. Rousseau and M. Dupuis, *J. Phys. Chem. C*, 2011, **115**, 7562–7572.
- 177 J. Tauc, R. Grigorovici and A. Vancu, *Phys. Status Solidi B*, 1966, **15**, 627–637.
- 178 R. A. Schoonheydt, *Chem. Soc. Rev.*, 2010, **39**, 5051–5066.
- 179 R. Zallen and M. P. Moret, *Solid State Commun.*, 2006, **137**, 154–157.
- 180 W. Hu, L. Li, G. Li, C. Tang and L. Sun, *Cryst. Growth Des.*, 2009, **9**, 3676–3682.
- 181 G. Yang and S. J. Park, *Materials*, 2019, **12**(12), 2003.
- 182 P. A. Morris Hotsenpiller, J. D. Bolt, W. E. Farneth, J. B. Lowekamp and G. S. Rohrer, *J. Phys. Chem. B*, 1998, **102**, 3216–3226.
- 183 J. L. Giocondi, P. A. Salvador and G. S. Rohrer, *Top. Catal.*, 2007, **44**, 529–533.
- 184 R. Hengerer, L. Kavan, P. Krtil and M. Grätzel, *J. Electrochem. Soc.*, 2000, **147**, 1467.
- 185 B. O'Regan and M. Grätzel, *Nature*, 1991, **353**, 737–740.
- 186 C. S. Kovash, J. D. Hoefelmeyer and B. A. Logue, *Electrochim. Acta*, 2012, **67**, 18–23.
- 187 M. Fischer, *Angew. Chem., Int. Ed. Engl.*, 1978, **17**, 16–26.
- 188 K. Zha, S. Cai, H. Hu, H. Li, T. Yan, L. Shi and D. Zhang, *J. Phys. Chem. C*, 2017, **121**, 25243–25254.
- 189 Y. Ding, I. S. Yang, Z. Li, X. Xia, W. I. Lee, S. Dai, D. W. Bahnemann and J. H. Pan, *Prog. Mater. Sci.*, 2020, **109**, 100620.
- 190 S. Ko, C. K. Banerjee and J. Sankar, *Composites, Part B*, 2011, **42**, 579–583.
- 191 S. F. Chen, J. P. Li, K. Qian, W. P. Xu, Y. Lu, W. X. Huang and S. H. Yu, *Nano Res.*, 2010, **3**, 244–255.

